



Contents lists available at ScienceDirect

Chemical Engineering Journal

journal homepage: www.elsevier.com/locate/cej

Programmed biomolecule delivery orchestrate bone tissue regeneration via MSC recruitment and epigenetic modulation

Zhuqing Wan, Qinyuan Dong, Yunsong Liu, Xiao Zhang, Ping Zhang, Longwei Lv^{*},
Yongsheng Zhou^{*}

Department of Prosthodontics, Peking University School and Hospital of Stomatology, National Engineering Research Center of Oral Biomaterials and Digital Medical Devices, National Clinical Research Center for Oral Diseases, Beijing Key Laboratory of Digital Stomatology, 22 Zhongguancun Avenue South, Haidian District, Beijing 100081, PR China

ARTICLE INFO

Keywords:

On-demand release
Bone regeneration
Stimuli-responsive hydrogel
Near-infrared
Small molecular drugs
Epigenetics

ABSTRACT

An on-demand delivery of chemotactic and osteogenic biomolecules to induce the recruitment and osteogenic differentiation of endogenous stem cells for *in situ* bone regeneration is appealing but challenging. To meet the changing demands at different periods of bone regeneration, a programmed delivery system was successfully fabricated by incorporating the near-infrared (NIR) light-responsive polydopamine-coated hydroxylapatite nanoparticles (nHA@PDA) into the thermo-responsive hydroxybutyl chitosan (HBC) hydrogel to regulate the therapeutic concentrations and time points of chemotactic simvastatin (SIM) and osteogenic pargyline (PGL). This smart hydrogel composite could perform an initial rapid release of SIM to meet the need of endogenous stem cell recruitment at the beginning of bone healing. Meanwhile, a flexible and NIR light-triggered increased release of PGL could promote osteogenic differentiation of migrated cells via a safe and stable epigenetic mechanism. Taken together, a well-orchestrated therapeutic timeline of two drugs was obtained in our programmed delivery system, thus enhancing bone regeneration in a highly effective method. In addition, the small molecular drugs utilized in this study were stable, safe, and easy for translation and clinical applications in bone tissue engineering.

1. Introduction

For decades, bone defects resulting from trauma or disease are treated by transplantation of autologous bone, which leads to a high incidence of complications including infection, necrosis, nerve damage, pain, and morbidity of donor site [1–3]. In current bone tissue engineering, efforts have been made to establish the co-delivery systems for multiple kinds of bioactive factors, which play crucial roles to modulate a cascade of events of bone regeneration [4–6]. Especially, there are two essential steps to accelerate bone tissue regeneration: one is the early-staged recruitment of stem cells to injured sites, another is the further osteogenic differentiation of migrated cells and the mineralization of extracellular matrix [7]. Considering the therapeutic effects of bioactive factors are mostly dose and time-dependent, it is appealing and necessary to deliver both chemotactic and osteogenic biomolecules in an on-demand and tunable manner to align with the natural bone healing cascades [8–11]. In current delivery systems, the most common strategy

to control the release timeline is to combine a rapid release of one biomolecule with a slow but sustained release of another via encapsulating them within multi-material-based or multi-layer-based compositions [11–14]. However, these systems still exist a lot of limitations to orchestrate the suitable concentration and therapeutic time points of biomolecules in an on-demand manner. Firstly, the release profiles of biomolecules mainly depend on their physical diffusion rates, which is usually concentration gradient-dependent [15]. Secondly, the release of different biomolecules also highly depends on a series of intrinsic properties of respective compositions in these systems, such as degradability, hydrophilicity, or surface charges [16–18]. Thirdly, these delivery systems often require complicated structural design and complex fabrication procedures to realize the efficiently spatial separation of biomolecules. The development of a more feasible, programmed, and controllable delivery system is still challenging.

The stimuli-responsive delivery systems have been reported for the on-demand release of therapeutic agents *in situ* [19–22]. Especially,

^{*} Correspondence authors at: Department of Prosthodontics, Peking University School and Hospital of Stomatology, 22 Zhongguancun Avenue South, Haidian District, Beijing 100081, PR China.

E-mail addresses: lvlw@bjmu.edu.cn (L. Lv), kqzhouysh@hsc.pku.edu.cn (Y. Zhou).

<https://doi.org/10.1016/j.cej.2022.135518>

Received 18 January 2022; Received in revised form 17 February 2022; Accepted 25 February 2022

Available online 28 February 2022

1385-8947/© 2022 The Authors.

Published by Elsevier B.V. This is an open access article under the CC BY-NC-ND license

(<http://creativecommons.org/licenses/by-nc-nd/4.0/>).

near-infrared (NIR) light-responsive delivery systems have been reported to control the on-demand release of biomolecules *in situ* and play efficient roles for anti-tumor or anti-infection treatments, while the controlled delivery of osteogenic biomolecules has rarely been reported [23–27]. Polydopamine (PDA) is a typical NIR light-responsive agent with suitable biocompatibility, photothermal conversion ability, and efficient drug loading and releasing capabilities [28,29]. By modifying with PDA coating, hydroxyapatite nanoparticles (nHA) with good osteoinductivity could serve as an efficient drug carrier under the control of NIR light [30–32]. Moreover, thermo-responsive hydrogels, which could perform “sol–gel” transformation under the physiological temperature, possess convenient manipulative flexibility without detrimental to living systems [33–36]. Among them, hydroxybutyl chitosan (HBC) has distinctive merits such as high water-content, porous microstructures, suitable biocompatibility, and fast “sol–gel” transformation, which facilitates the efficient rapid diffusion of bioactive factors at the early stage of bone repair in the programmed delivery system [36–38].

Meanwhile, the use of protein drugs, such as growth factors, as therapeutic agents in stimuli-responsive delivery systems has been limited due to their short half-life within the physiological microenvironment and low stability under the most of stimuli [39–41]. Instead, small molecular drugs with stabler and more efficient therapeutic effects could serve as potential alternatives to solve this limitation [42]. Our

previous studies found that simvastatin (SIM), a classical hypolipidemic agent, has promising chemotactic effect on mobilization, recruitment, and migration of endogenous mesenchymal stem cells (MSCs) at the early stage of bone healing [43,44]. In addition, our previous studies demonstrated that antihypertensive drug, pargyline (PGL), could promote the osteogenic differentiation of MSCs via epigenetic regulation [45,46]. It is worthwhile to explore their synergistic effects on osteogenesis and program the releasing concentration and time points of these biomolecules for bone tissue regeneration.

In this study, we aimed to design a programmed delivery system by combining the thermo-responsive HBC hydrogel with NIR light-responsive PDA coated nHA nanoparticles (nHA@PDA) for the on-demand release of chemotactic SIM and osteogenic PGL. Firstly, an initial burst release of SIM was designed to reach its therapeutic concentration rapidly and enhance the recruitment of MSCs. Meanwhile, the therapeutic concentration and time point of PGL could be controlled under the NIR light to facilitate the osteogenic differentiation of recruited MSCs (Fig. 1). Accordingly, we firstly validated the programmed release timeline of SIM and PGL, then investigated the *in vivo* stem cell recruitment and new bone formation capabilities of our programmed delivery system in the mice calvarial bone defect models. Especially, the flexible NIR light-triggered release profile and epigenetic regulation ability of PGL have been explored to confirm its osteogenesis

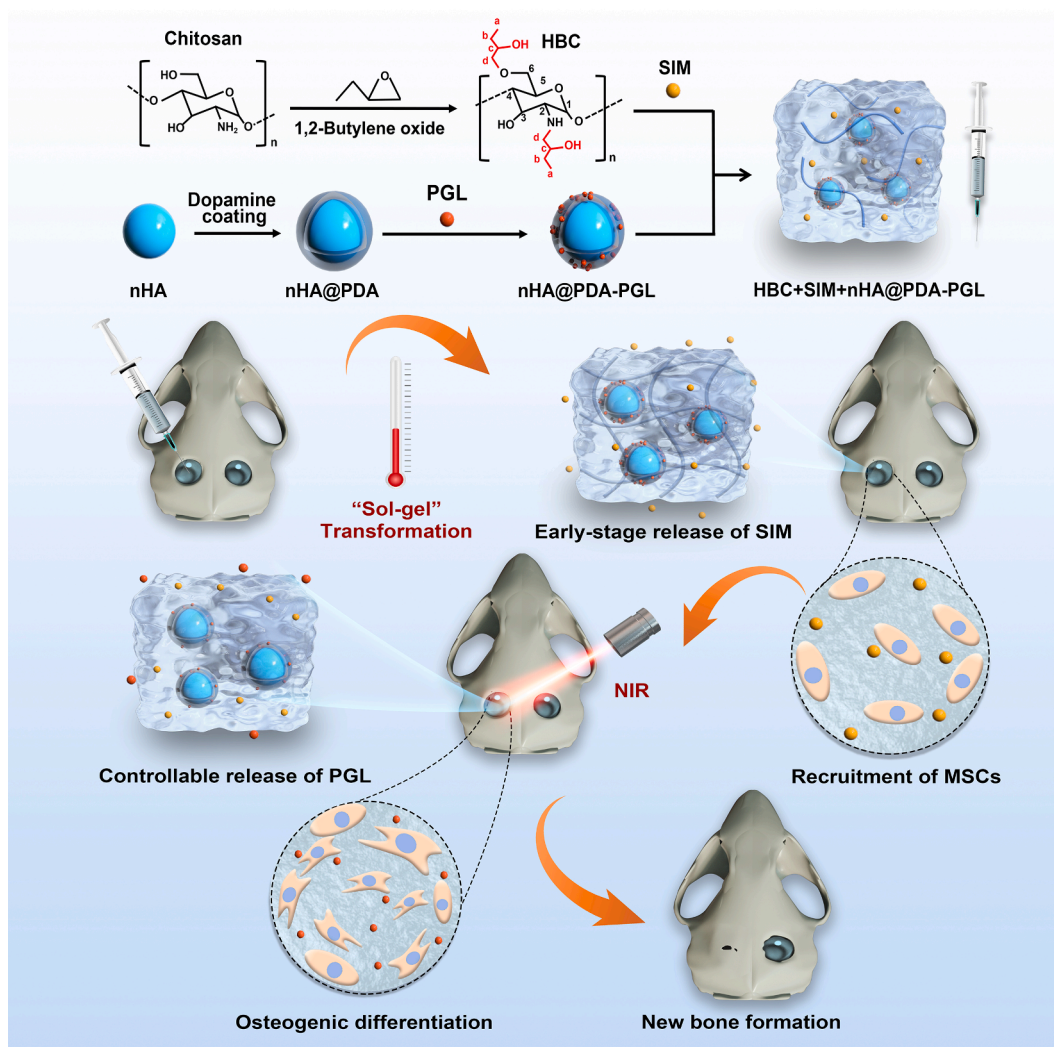


Fig. 1. Overview of our programmed delivery system with on-demand release of simvastatin (SIM) and pargyline (PGL) to orchestrate the processes in bone healing. An initial burst release of SIM could meet the demand of the recruitment of endogenous mesenchymal stem cells (MSCs). Meanwhile, the therapeutic time point of PGL could be controlled under the near-infrared (NIR) light irradiation to promote the osteogenic differentiation of recruited MSCs and new bone formation.

mechanism.

2. Materials and methods

2.1. Preparation of hydrogels composites

The freeze-dried HBC were sterilized under UV light irradiation for 2 h. The nanoparticles were sterilized by soaking in 75% ethanol for 2 h and freeze-dried. The formulated compositions of different hydrogel composites were shown in Table S1. Taking the HBC+SIM+nHA@PDA-PGL hydrogel for example, the 50 mg nHA@PDA-PGL nanoparticles were resuspended in 1 mL SIM solution (2 μ M) via vortexing for 5 min. Then 50 mg HBC was dissolve into above nanoparticles suspension under simultaneous stirring in ice water for 2 h, and kept at 4 $^{\circ}$ C overnight for further dissolving to obtain homogeneous mixed solutions. These mixtures were stocked at 4 $^{\circ}$ C for further use.

2.2. Rheological analysis

The rheological properties of the hydrogels were analyzed by parallel plate geometry using a Peltier plate on MARS 40 rheometer (Thermo HAAKE, Waltham, MA, USA). The diameter of the steel plate was 25 mm with a gap of 0.5 mm. The storage modulus (G') and loss modulus (G'') of samples were measured at 1% strain amplitude and 1 Hz and temperature range from 4 to 40 $^{\circ}$ C at a heating rate of 1 $^{\circ}$ C/min. The incipient gelation temperature (T_i) was defined as the time when G' and G'' were equivalent in value. Shear-dependence viscosity was measured at 25 $^{\circ}$ C and 37 $^{\circ}$ C in a shear rate range between 0.1 and 400 s^{-1} .

2.3. In vitro photothermal properties of hydrogel composites

The NIR photothermal ability of the HBC+SIM+nHA@PDA-PGL hydrogel was characterized by irradiating the hydrogels with the MDL-III-808 NIR laser (Changchun New Industries Optoelectronics Technology Co., Changchun, China) at 0.1, 0.2, 0.3 W/cm² for 3 min. The photothermal heating profiles were recorded by the 875-1i infrared thermal camera (Testo, MUN, Germany). Besides, the HBC+SIM+nHA@PDA-PGL hydrogel was repeatedly irradiated by the NIR laser for five cycles in the 6 min intervals (3 min on, 3 min off) to evaluate its photothermal stability. In addition, the temperature of HBC, HBC+nHA@PDA, HBC+SIM+nHA@PDA and HBC+nHA@PDA-PGL hydrogels were also periodically recorded at 0.2 W/cm² for 3 min.

2.4. In vitro cell migration assay

The primary mouse bone marrow-derived mesenchymal stem cells (mBMMSCs) purchased from the Procell (CP-M131, Wuhan, China) were used for all *in vitro* studies. At first, two different kinds of cell migration assays were performed to evaluate the chemotactic ability of SIM referring to the previous studies [9,39]. In Transwell assay, a total number of 2×10^4 mBMMSCs were resuspended in 100 μ L of serum-free α -MEM and placed in the upper chamber of a 24-well Transwell (Corning, 8 μ m). Then, 500 μ L of α -MEM (2% FBS) with different concentration of SIM (0.1 μ M, 0.2 μ M, 0.5 μ M, and 1.0 μ M) were added into the lower chamber. The group cultured with the SIM-free medium was used as the blank group. After cultured with 24 h, the mBMMSCs on the upper surface of chamber was wiped off with a cotton swab. The Transwell membrane was rinsed with PBS, and then fixed in methanol at room temperature for 30 min. For observation and quantitation, the cells were stained with 0.1% crystal violet solution. The migrated cells were observed in five random fields under 100 \times magnification and counted using Image J software.

Meanwhile, upward migration of mBMMSCs through a fibrin gel stimulated by SIM containing culture medium on top of the gel was evaluated. mBMMSCs were resuspended in 3 mg/mL fibrinogen solution (4×10^4 cells/mL). Fibrin gels were formed by adding 25 μ L of 1 mg/mL

thrombin solution and 475 μ L of cell-fibrinogen solution into 24-well plate. After gelation at 37 $^{\circ}$ C for 10 min, 500 μ L culture medium were added onto the top surface of fibrin gels (Fig. 5c. (i)). Four groups were set: blank (without drugs), SIM, PGL, SIM + PGL. For all groups, concentrations of SIM and PGL were 0.2 μ M and 0.2 mM respectively in α -MEM culture medium supplemented with 2% FBS. After cultured for 24 h and 72 h, the culture medium was removed, and gel was incubated with 2.5% glutaraldehyde for 15 min at 4 $^{\circ}$ C for fixation, then stained using DAPI for 5 min at room temperature for fluorescent staining. Cell distribution in the gels was imaged using 3D LSM710 confocal laser scanning microscope (CLSM) (Zeiss, Oberkochen, Germany) from bottom to top.

2.5. In vitro osteogenic differentiation of mBMMSCs

2.5.1. Alkaline phosphatase (ALP) activity

The details of cell culture were provided in [Supplementary material](#). ALP is a glycoprotein located on the cell surface and is widely recognized marker of osteoblast differentiation. After culturing for 7 days, the cells were fixed in 95% cold ethanol for 30 min and stained according to the manufacturer's protocol of a BCIP/NBT ALP staining Kit. Then images were obtained under microscopes or using a scanner. The ALP activity was evaluated using an ALP activity kit followed by the instruction and normalized to the total protein content of each sample.

2.5.2. Expression of osteogenic genes

Quantitative real-time polymerase chain reaction (qRT-PCR) assays reflecting on the gene expression were used to evaluate the osteogenic differentiation ability of mBMMSCs cultured with different hydrogel composites in the upper chamber of Transwell. Several osteogenic differentiation-related genes, such as runt related transcription factor 2 (*Runx2*), alkaline phosphatase (*Alp*), osteocalcin (*Ocn*) and collagen type I (*Col-1*) were further examined at 4 and 7 days. The total RNA was isolated with TRIzol reagent and measured via Nano Drop 8000 (Thermo Fisher Scientific Inc., MA, USA). Then, only those RNA with optical density ratio of 1.8–2.0 (260/280 nm) were reverse-transcribed to cDNA. qRT-PCR was conducted using the 7500 Real-Time PCR detection system (Applied Biosystems, Foster City, CA) with SYBR Green master mix (Roche Applied Science, Mannheim, Germany). Glyceraldehyde-3-phosphate dehydrogenase (*Gapdh*) was used for normalization. Primer sequences used in this study were listed in Table S2 in the [Supplementary material](#).

2.5.3. Immunofluorescence staining

The expression levels of bone specific proteins including RUNX2, OCN and COL-1 were evaluated using immunofluorescence staining. The mBMMSCs were cultured on glass slides in the lower chambers of 24-well Transwell plates and the hydrogels were injected into the upper chambers. The expression levels of bone specific proteins were observed by labeling the anti-RUNX2 antibody (1:1000) for 3 days and anti-OCN antibody (1:100) as well as anti-COL-1 antibody (1:1000) for 7 days, respectively, according to manufactures recommendations. Briefly, the samples were fixed using 4% paraformaldehyde solution for 30 min, permeabilized with 0.25% triton X-100 for 7 min, and blocked in 0.8% bovine serum albumin (BSA) for 1 h. After that, the samples were incubated at 4 $^{\circ}$ C overnight with primary antibodies, washed, and the TRITC conjugated IgG (1:100) was added. All the samples were counterstained for F-actin using FITC conjugated phalloidin, stained with DAPI for the nucleus and finally imaged under the LSM710 CLSM.

2.6. In vivo bone regeneration and MSC recruitment assessment

2.6.1. Surgical procedure and hydrogels injection

C57BL/6 mice (6-weeks-old, male, 18–20 g) were used for *in vivo* studies. All animal experiments were approved by the Peking University Animal Care and Use Committee (Project Number: LA2021040) and

performed in accordance with the institutional animal guidelines. A critical sized calvarial bone defect model was used to evaluate the stem cell recruitment and osteogenesis abilities of hydrogel composites in this study [34,47–49]. After general anesthesia administration and disinfection, a sagittal incision was made to expose the calvarium of mice. Periosteum covering the bone was removed and two circular full-thickness bone defects, each with a diameter of 3 mm, were created on the bilateral parietal bone of mouse by using a trephine bur under low-speed drilling and copious saline irrigation. The bone debris was removed carefully without the damage to the underlying dura mater. Two defects in each mouse were injected with 100 μL same hydrogel composite. Hydrogel composites were prepared as listed in Table S1 and stored on ice before injection. Finally, the incision sites were sutured with 6–0 nylon sutures.

2.6.2. Analysis of bone regeneration *in vivo*

At first, to evaluate the osteogenic abilities of different hydrogel composites, 24 animals were randomly divided into six groups: (1) blank group (without hydrogel); (2) HBC+nHA@PDA hydrogel; (3) HBC+SIM+nHA@PDA hydrogel; (4) HBC+nHA@PDA-PGL hydrogel + NIR light irradiation; (5) HBC+SIM+nHA@PDA-PGL hydrogel; (6) HBC+SIM+nHA@PDA-PGL hydrogel + NIR light irradiation ($n = 8$ defects per group). Eight weeks after surgery, the animals were euthanatized and then calvarial bones were harvested for micro-computerized tomography (micro-CT) scanning and histological evaluation. The experimental procedures and details were shown in [Supplementary material](#).

In addition, to investigate the *in vivo* bone formation influenced by the simultaneous or programmed release of SIM and PGL, animals were randomly assigned as three groups: (1) control group (repaired with HBC+nHA@PDA hydrogel), (2) simultaneous release group (repaired with HBC+SIM+PGL+nHA@PDA hydrogel), (3) programmed release group (repaired with HBC+SIM+nHA@PDA-PGL hydrogel + NIR light irradiation) ($n = 10$ defects per group). Twelve weeks after surgery, the animals were euthanatized and then calvarial bones were harvested for micro-CT scanning and histological evaluation.

2.6.3. *In vivo* MSC recruitment assessment

The capacity of hydrogels to recruit host MSCs *in vivo* was assessed using immunofluorescence staining and flow cytometric analysis. The calvarial defect model of C57BL/6 mice was established as previous. Four kinds of hydrogels were applied to repair the calvarial bone defects as follows: (1) HBC+nHA@PDA hydrogel, (2) HBC+SIM+nHA@PDA hydrogel, (3) HBC+nHA@PDA-PGL hydrogel, (4) HBC+SIM+nHA@PDA-PGL hydrogel ($n = 6$ defects per group). Three days after injection, three calvarial samples of each group were harvested and fixed in 4% paraformaldehyde and decalcified with 12% EDTA (pH 7.4). Frozen sections (5 μm) of samples were blocked with 5% BSA for 30 min at 37 °C and then stained with Alexa Fluor® 488-labeled CD90 antibody and Cy3-labeled CD44 antibody at 4 °C overnight. Afterwards, the samples were counterstained with DAPI to label the nuclei and imaged by LSM880 CLSM (Zeiss, Oberkochen, Germany). The cells in defect area were identified as MSCs when they stained double-positive for the mesenchymal marker CD90 (green) and CD44 (red). The numbers of MSCs in the defect area were measured using Image J software.

The percentages of recruited MSCs in defect areas were further analyzed via flow cytometry ($n = 3$ mice per group). Three days after implantation, fraction type of non-hematopoietic MSCs to the defect areas was analyzed by cytometry after staining with 4 monoclonal antibodies including anti-CD45, anti-TER119, anti-CD44 and anti-CD90 (Biolegend, San Diego, CA, USA). Briefly, the hydrogels and surrounding calvarial bone tissues were fragmented using a surgical scissor, washed with buffer solution, incubated in 1.5 mg/mL Type II/IV collagenase (Gibco, Thermo Fisher Scientific Inc., MA, USA) for 30 min at 37 °C and filtered through 40 μm cell strainer. The red blood cells were lysed and the cells were stained with anti-bodies on ice for 30 min. The

flow cytometric experiments were performed on the CytoFlex LX flow cytometer (Beckman Coulter, Inc. Boulevard Brea, CA, USA). Data were analyzed using Flowjo 10.6.2 software (Tree Star, San Carlos, CA, USA).

2.7. Analysis of epigenetic mechanism

2.7.1. Immunofluorescence staining

The epigenetic mechanism was firstly evaluated via immunofluorescence staining. As described above, mBMMSCs were cultured on glass slides in the lower chambers of 24-well Transwell plates (Corning, 0.4 μm) with 100 μL HBC+nHA@PDA and HBC+nHA@PDA-PGL hydrogels injected into the upper chambers. The NIR light irradiation was performed in HBC+nHA@PDA-PGL group at day 3. To examine the methylation of histone H3 at lysine 4 (H3K4), the samples were incubated with 1:1000 H3K4me1, H3K4me2 and H3K4me3 primary antibodies after washed, fixed, permeabilized and blocked at 7 days of culture. Then the incubation of TRITC conjugated secondary antibody, FITC conjugated phalloidin, and DAPI was performed. The immunofluorescence images were taken under the LSM710 CLSM.

Furthermore, the expression levels of methylation of H3K4 *in vivo* were evaluated via immunofluorescence staining as described above. The calvarial tissues in HBC+nHA@PDA and HBC+nHA@PDA-PGL+NIR groups ($n = 6$ defects per group) were harvested after 14 days of injection and stained with Cy3-labeled H3K4-methylation antibody and DAPI. The immunofluorescence images were taken under the LSM880 CLSM.

2.7.2. Chromatin immunoprecipitation (ChIP) assay

ChIP assay was performed using a ChIP assay kit (Beyotime, Nanjing, China). The cell culture was performed using Transwell methods as above. mBMMSCs were seeded into the lower chambers of six-well Transwell plates (Corning, 0.4 μm) and 200 μL hydrogels were injected into the upper chambers. At day 3, 7 and 11, the HBC+nHA@PDA-PGL+NIR group was irradiated with an 808 nm NIR light (0.2 W/cm², 3 min, 3 times). Briefly, after cultured for 14 days, mBMMSCs cells were cross-linked with 1% formaldehyde, terminated with glycine, lysed, and sonicated on ice. The sonicated DNA fragments were incubated with H3K4me2, non-specific rabbit IgG and H3 antibodies overnight and then incubated with protein A/G agarose at 4 °C for 6 h. Finally, immune complexes were captured by protein A/G agarose and eluted with elution buffer (1% SDS, 0.1 M NaHCO₃). Cross-linked DNA were reversed at 65 °C for 4 h in a high salt buffer (0.2 M NaCl, 50 mM Tris, pH 6.5, 10 mM EDTA, and 0.2 mg/ml proteinase K) and purified using DNA purification kit. Finally, the extracted immunoprecipitated DNA fragments were quantified by real-time PCR. The primer pairs used in this study were as follows: mouse *Runx2* promoter, (forward) 5'-GAGACAGAGGAACACCCATAAG-3' and (reverse) 5'-CTTCCCTCCCTCTTTCTCAATC-3'; mouse *Ocn* promoter, (forward) 5'-GAGAGTTGGAGCCAGTTTATC-3' and (reverse) 5'-TACTCC-TACTGTGTCTCTC-3'.

2.8. Statistical analysis

All data were analyzed via SPSS 19.0 software (SPSS Inc., Chicago, IL, USA). The statistical analysis between two groups were performed using independent two-tailed Student's *t* tests. One-way analysis of variance (ANOVA) followed by a Tukey-Kramer post hoc test was used to analyze the difference between more than two groups. Statistical significance was accepted for $P < 0.05$, and reported as follows: * $P < 0.05$, ** $P < 0.01$.

3. Results

3.1. Synthesis and characterization of HBC

HBC was synthesized by connecting the ring-opening product of 1,2-

butane oxidation to the chitosan molecular chain under alkaline conditions. In this study, the degree of hydroxybutyl substitution assessed by elemental analysis was 1.88 (Table S3). The ^1H nuclear magnetic resonance (NMR) spectrum of HBC dissolved in deuterium oxide (D_2O) was presented in Fig. S1a. The peaks at 0.9 and 1.5 ppm were assigned to $-\text{CH}_3$ and $-\text{CH}_2-$ of the hydroxybutyl moiety, respectively. Moreover, the ratio of the integrated areas of these new peaks was 3:2, which indicated that the hydroxybutyl groups have successfully conjugated on the chains of chitosan. The peaks from 3.5 to 4.0 ppm attributed to the non-anomeric protons (H3-6). The resonances from 2.5 to 3.0 ppm were assigned to the three protons of N-acetyl glucosamine and the proton of glucosamine residues (H2). Meanwhile, the ^1H NMR spectra of chitosan and HBC dissolved in 10% deuterated hydrochloric acid (DCl) in D_2O were present in Fig. S1c. New signal at 0.4 and 1.0 ppm (which were not observed for chitosan) were assigned to $-\text{CH}_3$ and $-\text{CH}_2-$ of the hydroxybutyl moiety, respectively.

The Fig. S1b showed the fourier transform infrared spectroscopy (FTIR) results of chitosan and HBC. Compared to the spectrum of the original chitosan, the spectrum of the HBC showed new absorption peaks at $2876\text{--}2920$ and 1462 cm^{-1} , which corresponded to the C-H stretching and bending of the $-\text{CH}_3$ group of the hydroxybutyl moiety, respectively. The absorption peaks at 1023 cm^{-1} in chitosan spectrum was contributed to the C-O stretching vibration of C6-OH. This peak was enhanced and shifted into double-peak at $1026\text{--}1054\text{ cm}^{-1}$ in the HBC spectrum, implying that hydroxybutyl group introduction mainly at the C6-OH position.

3.2. Physical characterizations of nHA@PDA and hydrogels composites

Fig. 2a and Fig. S2c showed the transmission electron microscopy (TEM) and scanning electron microscopy (SEM) images of the nHA and

nHA@PDA, respectively. The diameter of nHA was approximately $38.03 \pm 10.51\text{ nm}$, which was similar to the diameters of natural bone nanocrystals [50,51]. The TEM images showed that there was a uniform PDA coating ($\sim 8\text{ nm}$) appeared on the surface of nHA, and the diameter of nHA@PDA revealed an increased size to about $54.66 \pm 10.60\text{ nm}$ after coating process. In addition, as shown in the UV-Vis spectra (Fig. S2c), the absorbance of PGL at 262 nm could be observed in the samples of PGL and nHA@PDA-PGL solutions. The drug loading content on the PGL-loaded nHA@PDA (nHA@PDA-PGL) was $9.58 \pm 0.46\%$. Besides, the zeta potential of the nHA@PDA increased from $-16.77 \pm 0.65\text{ mV}$ to $-10.83 \pm 0.42\text{ mV}$ after the PGL loading (Fig. 2b). These results indicated the successful loading of PGL on the nHA@PDA nanoparticles.

Thereafter, different hydrogel composites were successfully prepared by mixing the SIM as well as nHA@PDA nanoparticles with or without the loading of PGL into the thermo-responsive HBC hydrogel, and their compositions and abbreviations were listed in Table S1. The structure and physical characterizations of three typical hydrogel composites (pure HBC hydrogel, nanoparticles containing HBC+nHA@PDA hydrogel as well as drugs-loaded HBC+SIM+nHA@PDA-PGL hydrogel) were further investigated. At first, the sol-gel transition of hydrogels was observed via a tube inversion method (Fig. 2c). It can be observed that the aqueous solution of the pure HBC was transparent at low temperature and became turbid after incubated at $37\text{ }^\circ\text{C}$. The hydrogels became dark with the incorporation of nanoparticles. The "sol-gel" transition occurred within 3 min at $37\text{ }^\circ\text{C}$. Besides, the SEM images (Fig. 2c) revealed that HBC hydrogel without nanoparticles had a looser internal micro-structure with an average pore size around $99.06 \pm 22.83\text{ }\mu\text{m}$. After adding nHA@PDA or nHA@PDA-PGL nanoparticles, the wall of gels was homogenously embedded with many grains, which could be nanoparticles and their aggregates. The pore sizes of the hydrogels were slightly reduced to $92.71 \pm 27.41\text{ }\mu\text{m}$ (HBC+nHA@PDA

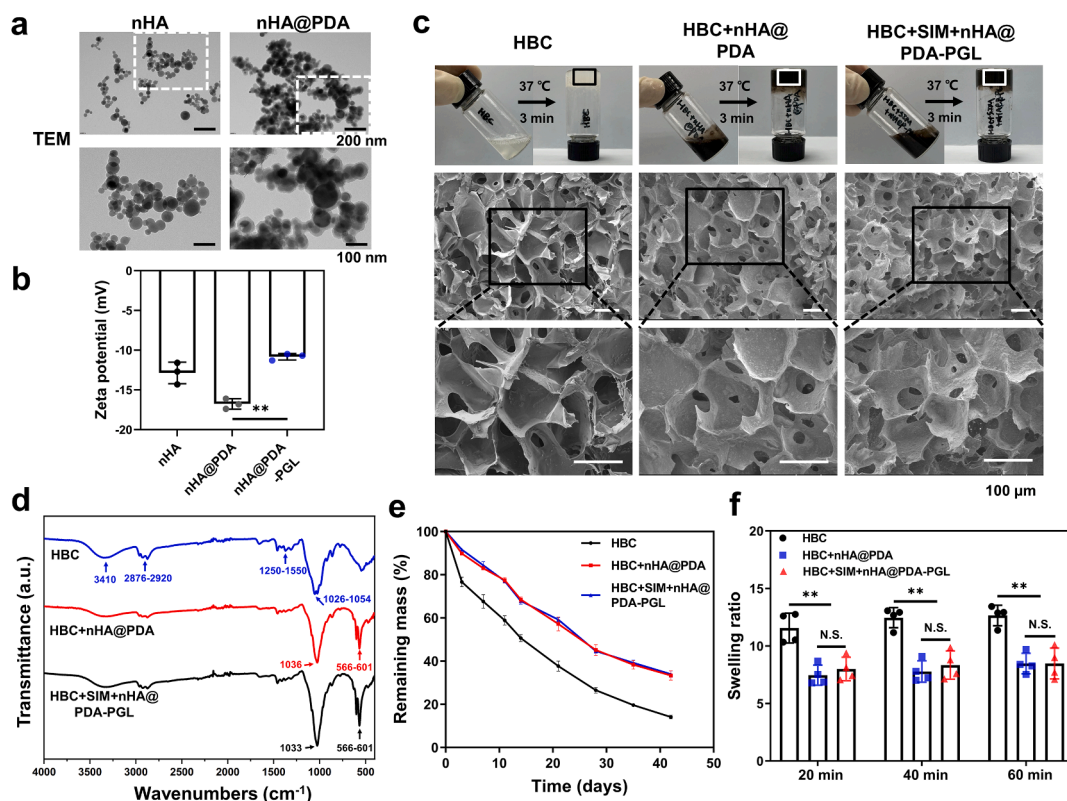


Fig. 2. Characterizations of hydrogel composites. (a) TEM images of hydroxylapatite nanoparticles (nHA) and polydopamine-coated hydroxylapatite nanoparticles (nHA@PDA). (b) Zeta potentials of nHA, nHA@PDA, and nHA@PDA loaded with pargyline (nHA@PDA-PGL) nanoparticles. (c) Photographs denoted the inceptive mixtures and the terminative gels after incubated in $37\text{ }^\circ\text{C}$ for 3 min as well as SEM images showing the internal microstructures of different hydrogel composites after freeze-dried. (d) FTIR spectra of different hydrogel composites. (e) Degradation degrees of different hydrogel composites in PBS solution ($n = 6$ per group). (f) Swelling ratios of different hydrogel composites in PBS solution ($n = 4$ per group, N.S. no significance, **: $P < 0.01$).

hydrogel) and $85.69 \pm 32.76 \mu\text{m}$ (HBC+SIM+nHA@PDA-PGL hydrogel). Meanwhile, the energy-dispersive spectroscopy (EDS) spectrums of hydrogels (Fig. S2a) were recorded to identify their element composition. The elemental mapping images (Fig. S2b) illustrated that the Ca and P elements were uniformly distributed in both HBC+nHA@PDA and HBC+SIM+nHA@PDA-PGL hydrogels, which representatively confirmed the uniform distribution of nHA@PDA nanoparticles.

The Fig. 2d showed the FTIR spectra of hydrogel composites. Compared to the spectrum of the HBC, the sharp adsorption peak at around $1033\text{--}1036 \text{ cm}^{-1}$ and the characteristic spectra bands at $566\text{--}601 \text{ cm}^{-1}$ were attributed to the components of ν_3 antisymmetric P-O stretching mode and ν_2 O-P-O bending mode of hydroxyapatite in nHA@PDA containing hydrogels. The absorption peak from 1250 cm^{-1} – 1550 cm^{-1} was considered as the stretching vibration and asymmetric deformation of C–H bond of aromatic structures in composites. The broad band at 3410 cm^{-1} was the characteristic peak of the –OH and N–H groups of HBC and catechol groups of PDA coating, which mainly helping the formation of hydrogen bonds. Meanwhile, the abundant aromatic structures and catechol groups of the hydrogel composites may contribute to their potential application in drug loading and releasing.

The *in vitro* biodegradation profiles of hydrogel composites were shown in Fig. 2e. The degradation rate of pure HBC hydrogel was significantly faster than nanoparticles containing hydrogels by about 20% because that nHA has slow degradation rate [52–54]. In addition, the abundant active groups, such as catechol, amine, and imine groups, on PDA coating of nanoparticles could afford secondary adhesion reactions with chains of HBC and increase their crosslinking density, leading to a decreased degradation rate of hydrogel [55–57]. The weight loss of HBC hydrogel was more than 80% after immersing in PBS for 42 days, while the remaining mass ratio of nanoparticles containing hydrogels decreased by 65% within 42 days. There was no obvious difference in the degradation behaviors between nHA@PDA containing hydrogels with or without drugs loading.

Meanwhile, both HBC hydrogel and nanoparticles modified hydrogels exhibited high swelling ratio (Fig. 2f), which indicated high porosity and ideal water absorption performance of gels. The introduction of hydroxybutyl groups facilitate the formation of hydrogen bonds between the chains of HBC and water molecules, resulting in more

water absorption. Compared to the pure HBC hydrogel, the nanoparticles modified hydrogel composites displayed a declined swelling ratio, which may due to that abundant functional groups on PDA coating enhanced the interactions between hydrogel networks and lead to a better structural stability [58–60].

3.3. Rheological properties of hydrogel composites

The thermo-responsive abilities of hydrogel composites were investigated via rheometric measurements. The incipient gelation temperature (T_i) of different hydrogels was determined via temperature-dependent functions of G' and G'' in Fig. 3a and listed in Table S4. The T_i of HBC hydrogel was $22.56 \text{ }^\circ\text{C}$ while T_i of nHA@PDA containing hydrogels tended to decrease. The gap between the G' and G'' curves in gels incorporated with nanoparticles became smaller when compared with the HBC gel, suggesting that incorporation of nanoparticles would enhance the elasticity of mixtures. To further investigate the injectabilities of hydrogels, the viscosity variation against shear rate (Fig. S3a and Fig. S3b) was measured at $25 \text{ }^\circ\text{C}$ and $37 \text{ }^\circ\text{C}$, respectively. The viscosity of all samples decreased sharply with the increasing shear rate, indicating the shear thinning behavior of the hydrogel composites.

3.4. *In vitro* photothermal properties of hydrogel composites

At first, the photothermal effects of HBC+SIM+nHA@PDA-PGL hydrogel composite at different NIR power densities were observed (Fig. 3b). After irradiation under 808 nm NIR light at different densities of 0.10, 0.20, and 0.30 W/cm^2 for 3 min, the temperature increase of HBC+SIM+nHA@PDA-PGL hydrogel finally reached 5.2, 8.6 and $15.6 \text{ }^\circ\text{C}$, respectively. Considering that hyperthermia (above $50 \text{ }^\circ\text{C}$) may cause normal cell/tissue necrosis [27,61,62] and physiological temperature of body is about $37 \text{ }^\circ\text{C}$, the temperature increase should be controlled around $8 \text{ }^\circ\text{C}$ and the laser density of 0.20 W/cm^2 was selected for the following *in vitro* and *in vivo* experiments. The Fig. S2d showed that there was no obvious difference within the photothermal effects of nHA@PDA containing hydrogels with different drugs loading under the same density of NIR light irradiation (0.20 W/cm^2), indicating the SIM and PGL did not impact on the photothermal properties of

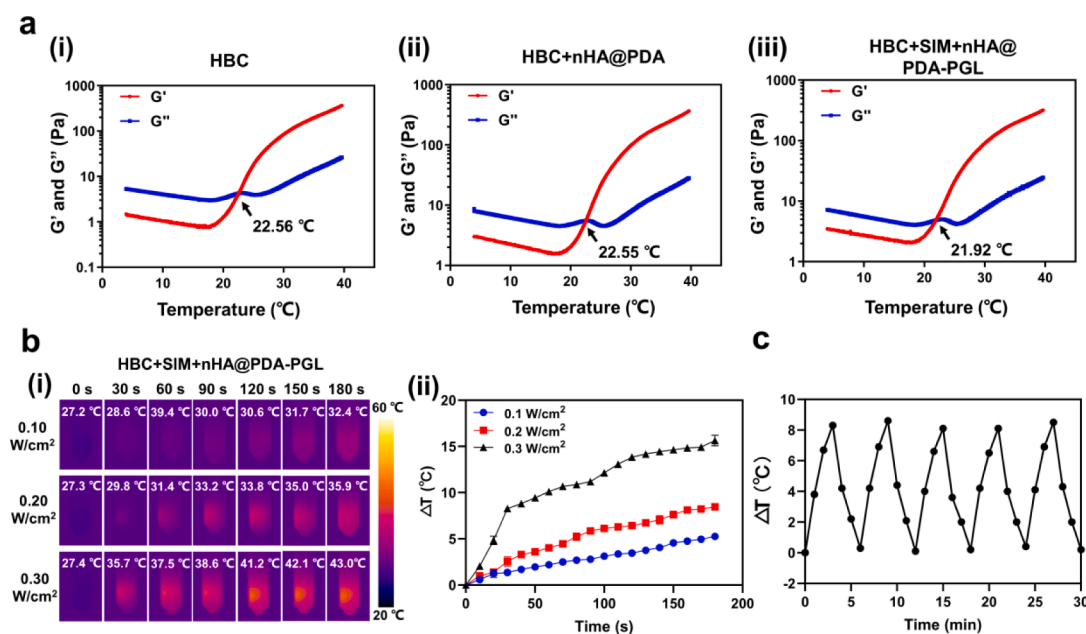


Fig. 3. Stimuli-responsive properties of hydrogel composites. (a) Typical temperature-dependent functions of storage modulus (G') and loss modulus (G'') for HBC (i), HBC+nHA@PDA (ii), and HBC+SIM+nHA@PDA-PGL (iii) hydrogel composites. (b) Photothermal property evaluation of HBC+SIM+nHA@PDA-PGL hydrogel. Infrared thermal images (i) and temperature changes (ii) of HBC+SIM+nHA@PDA-PGL hydrogel at different NIR power densities (808 nm, 0.10, 0.20, and 0.30 W/cm^2 , 3 min). (c) Temperature changes of HBC+SIM+nHA@PDA-PGL hydrogel over 5 irradiation cycles (808 nm, 0.2 W/cm^2 , 3 min on, 3 min off, 6 min intervals).

HBC+SIM+nHA@PDA-PGL hydrogel. Furthermore, it was observed that no decline in the maximum temperature of HBC+SIM+nHA@PDA-PGL hydrogel over five irradiation cycles (Fig. 3c), indicating the excellent photothermal stability of hydrogel composites.

3.5. The release profiles of SIM and PGL from hydrogel composites

At first, we investigated the release profile of SIM and the loading concentration of SIM in hydrogel composite was 2 μM . As shown in Fig. 4a, an initial burst release of SIM was observed from HBC+SIM+nHA@PDA hydrogel and the release of SIM could quickly reach about 0.2 μM within the first 3 days, which was consistent to the therapeutic concentration of SIM and may facilitate its chemotactic effect at the early-stage of bone repair. Most of SIM could be efficiently released within the first 7 days in two groups, followed by a slow and limited release of SIM during the next 3 weeks. Meanwhile, the NIR light irradiation may slightly increase the release of SIM by 6% at the end of 28 days of observation.

To confirm the NIR light triggered release of PGL, we investigated the release profiles of PGL from HBC+nHA@PDA-PGL hydrogel with or without NIR light irradiation (Fig. 4b). Firstly, a mild release of PGL could be observed before NIR light irradiation. Thereafter, a significant increased release of PGL could be detected after NIR light irradiation at the day 3, 7 and 11, respectively, which could maintain the optimal therapeutic concentration of PGL (0.2 to 0.3 mM) within 21 days (Table S5). On the contrary, the group without NIR light irradiation performed a slow and decreased release with time and resulted in an insufficient concentration of PGL after 7 days of observation (Table S5). In addition, we also evaluated the release kinetics of PGL from HBC+PGL+nHA@PDA hydrogel. The results showed that there was a fast and burst release of PGL within the first 10 days (Fig. 4b, blue line), leading to a high concentration of PGL (about 0.8 mM) at the beginning of releasing (Table S5). Then a sharply slower release of PGL could be observed during the next 3 weeks. Among the three different release manners, a flexible and on-demand release of PGL could be obtained via using the nHA@PDA as the drug carrier and regulating the release time point of PGL under the control of NIR light irradiation.

These results indicated that a well-orchestrated programmed release of SIM and PGL could further obtain from HBC+SIM+nHA@PDA-PGL hydrogel under the control of NIR light, and a burst and simultaneous release of two drugs may occur when directly applying HBC hydrogel itself as the drugs reservoir in HBC+SIM+PGL+nHA@PDA hydrogel.

3.6. Cell culture and cell viability assay

The mBMMSCs were seeded on the surface of HBC hydrogel and their proliferation was evaluated via live/dead staining assay on day 1, 3 and 7 (Fig. S4a). There were no obvious dead cells in the HBC group and no

obvious difference in cell density between the group without hydrogels (blank) and HBC group at each time point, suggesting the HBC hydrogel did not influence the cell viability and proliferation of mBMMSCs. Furthermore, the biocompatibility of different nanoparticles containing hydrogel composites were tested. The live/dead staining (Fig. 5a) demonstrated that the numbers of live cells on the drugs loading hydrogel composites were similar to that on the HBC+nHA@PDA hydrogel and blank group. After culturing for 3 and 7 days, the viable cells in all groups had remarkably higher density than that on day 1, visually demonstrating that cells cultured on hydrogels have already significantly proliferated. No obvious cytotoxicity could be observed in different nanoparticles containing hydrogel composites. Moreover, the short-time NIR light irradiation on day 3 and 7 had no obvious influence on cell adhesion and proliferation, indicating that the well moderated photothermal effect of hydrogel composite was harmless to mBMMSCs *in vitro*.

3.7. *In vitro* mBMMSC recruitment by SIM

In order to optimize the SIM dose for *in vitro* mBMMSC recruitment, the chemotactic effects of different concentrations of SIM had been preliminarily evaluated via Transwell migration assay (Fig. S4b). The results showed that SIM exerted a concentration-dependent effect on *in vitro* mBMMSC recruitment. The number of migrated mBMMSC increased with the increasing concentration of SIM from 0 μM to 0.2 μM , while this chemotactic effect became weaker under the higher concentration of SIM. The most efficient chemotactic concentration is at 0.2 μM , which was consistent to our previous studies [44,63]. Furthermore, we evaluated the *in vitro* chemotaxis of mBMMSCs by SIM, PGL and combination of both. As shown in Fig. 5b, more cell migrated to the lower chamber in the SIM group than the PGL group after 24 h of culture, representing that SIM alone exerted superior chemotactic effect compared to PGL alone. The mBMMSCs cultured with both SIM and PGL also performed significant chemotaxis, indicating that SIM played the certain role in the recruitment of mBMMSCs. In addition, Fig. 5c showed the upward migration of mBMMSCs stimulated by SIM and PGL in fibrin gels. The mBMMSCs started to migrate upward in gels after cultured for 24 h in SIM containing groups and most of mBMMSCs completed the migration to the top of fibrin gels at 72 h. While, the mBMMSCs in groups without SIM had no obvious migration and distributed uniformly in fibrin gels. These results verified the efficient chemotactic ability of low dose SIM *in vitro*.

3.8. *In vitro* osteogenic induction abilities of different hydrogel composites

The results of ALP staining and quantification (Fig. S4c) demonstrated that mBMMSCs cultured with 0.2 mM PGL exhibited the strongest ALP activity compared with the other concentrations of PGL. The

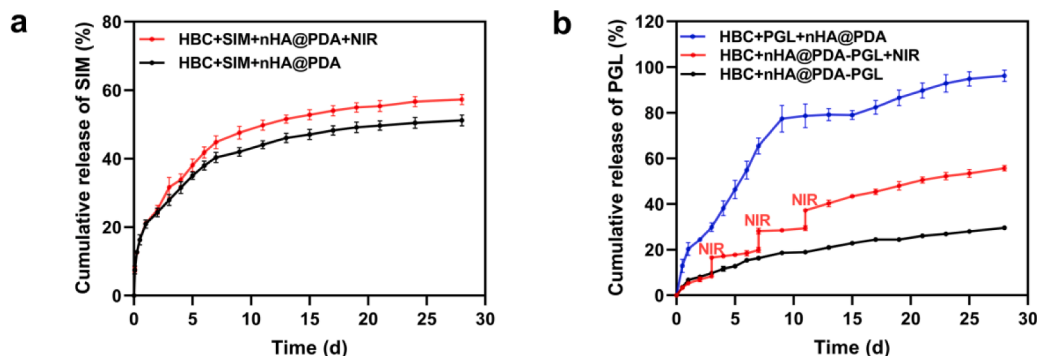


Fig. 4. Programmed release profiles of SIM and PGL from hydrogel composite. (a) *In vitro* drug release profile of SIM from HBC+SIM+nHA@PDA hydrogel composite (red: with NIR light irradiation, black: without NIR light irradiation). (b) *In vitro* drug release profile of PGL from HBC+nHA@PDA-PGL hydrogel composite (red: with NIR light irradiation, black: without NIR light irradiation) and HBC+PGL+nHA@PDA hydrogel composite without NIR light irradiation (blue).

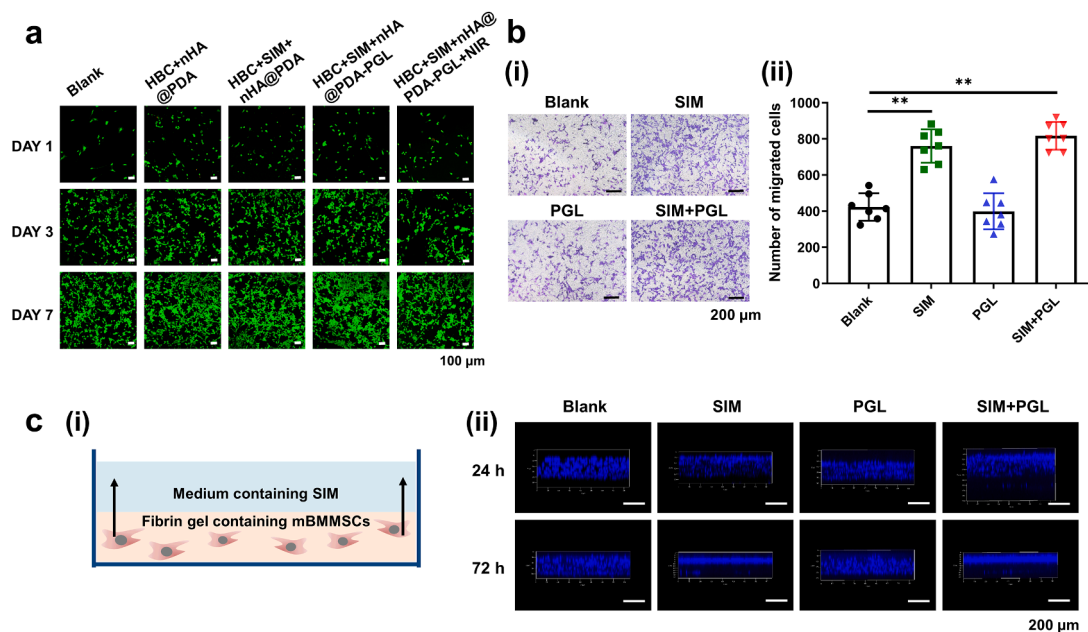


Fig. 5. The biocompatibilities of hydrogel composites and the *in vitro* mBMMSC recruitment ability of SIM. (a) Live/dead staining of mBMMSCs after cultured on different hydrogel composites for 1, 3 and 7 days. Living cells were stained with calcein-AM in green and dead cells were stained with propidium iodide in red. (b) Transwell chemotaxis assay of mBMMSCs cultured with SIM and PGL. The cells that migrated to the lower chamber were stained with crystal violet (i) and the number of migrated cells per microscopic field were counted using Image J software (ii) ($n = 7$, **: $P < 0.01$). (c) (i) Illustration of the upward migration of mBMMSCs through the fibrin gels. (ii) 3D images of the fibrin gels were scanned from the bottom to the top and the nuclei of mBMMSCs were stained with DAPI.

ALP activity increased with the increasing concentrations of PGL from 0.05 to 0.2 mM. However, the ALP activity decreased when the concentrations increased to 0.5 and 1.0 mM, indicating that the osteogenic ability of PGL was concentration-dependent. It was essential to control the concentration of PGL to optimize its osteogenic ability.

To investigate the *in vitro* osteogenic induction abilities of different hydrogel composites, the ALP staining of migrated mBMMSCs after 7 days of culture was evaluated (Fig. 6b). All groups cultured with SIM loaded hydrogels displayed higher levels of positive staining and activity in favor of the chemotactic effect of SIM with more migrated mBMMSCs. Among them, the HBC+SIM+nHA@PDA-PGL group with NIR light irradiation expressed the highest level of positive staining and activity, which evidenced the best osteogenic ability. The NIR light-responsive hydrogel composites could control the release of PGL, maintain the concentration of PGL within the suitable range and significantly promote the ALP activity. Besides, a quantitative analysis of ALP activities was presented in Fig. 6b, which also in accordance with the staining results.

The expression levels of bone-related genes, such as *Runx2*, *Alp*, *Ocn* and *Col-1*, were measured and presented in Fig. 6d. Compared with the HBC+nHA@PDA group, the SIM containing hydrogel composites groups slightly enhanced the expression of osteogenic genes in mBMMSCs. Meanwhile, groups with NIR light-controlled release of PGL (HBC+nHA@PDA-PGL+NIR, HBC+SIM+nHA@PDA-PGL+NIR groups) exhibited higher upregulated expression levels of osteogenic genes. Specially, the HBC+SIM+nHA@PDA-PGL+NIR group with the programmed release of SIM and PGL showed much higher upregulated gene expression levels of *Alp* (2.06-fold), *Runx2* (2.19-fold), *Ocn* (1.81-fold), *Col-1* (3.20-fold) compared with the group without drug loading after 7 days of culture.

Furthermore, the potent expression levels of RUNX2 (the early marker of osteogenic maturation), OCN and COL-1 (later markers of osteogenic differentiation and mineralization) in mBMMSCs were confirmed via immunofluorescence staining (Fig. 6e, f). Similarly, the expression of osteogenic genes, the mBMMSCs in groups with the NIR light-controlled release of PGL, exhibited higher levels of RUNX2 (3

days), OCN, and COL-1 (7 days) expression than groups without the loading of PGL. Among them, the mBMMSCs cultured in the HBC+SIM+nHA@PDA-PGL+NIR group with programmed release of SIM and PGL had the highest up-regulated expression levels of these osteogenesis-related proteins.

In general, our *in vitro* results showed that the HBC+SIM+nHA@PDA-PGL hydrogel composite with the programmed release manner owned the strongest ability to induce the osteogenic differentiation of mBMMSCs *in vitro*, which mainly attributing to the NIR light-controlled release of PGL from the hydrogel composite and the synergistic effect combined with the released SIM. The low concentration of SIM released from the hydrogel composites could slightly enhanced the osteogenic differentiation of mBMMSCs but not so obvious compared with the released PGL.

3.9. *In vitro* osteogenic induction abilities of hydrogel composites influenced by the simultaneous or programmed release of SIM and PGL

Furthermore, we investigated the osteogenic induction abilities of PGL-loaded hydrogel composites with simultaneous or programmed release of SIM and PGL. The total dose of PGL in two kind of hydrogel composites was same (5 mM). ALP staining and quantification showed that the programmed release group (HBC+SIM+nHA@PDA-PGL+NIR) exhibited the significantly higher level of ALP activity than control group (HBC+nHA@PDA) and simultaneous release group (HBC+SIM+PGL+nHA@PDA) (Fig. 7a, b). Meanwhile, the expression levels of osteogenesis-related genes, such as *Alp*, *Runx2*, *Ocn* and *Col-1* were significantly up-regulated at 4 d and 7 d in programmed release group (Fig. 7c). In simultaneous release group without NIR light-controlled release of PGL, the expression levels of genes were moderately increased compared with the control group without drug loading, yet still lower than the programmed release group. Moreover, the protein expression levels of the RUNX2, OCN and COL-1 were analyzed at the specific time periods (Fig. 7d, e). The fluorescent images exhibited that higher RUNX2 expression (3 days) was observed in programmed release group compared with other two groups. Imaging at the end of 7

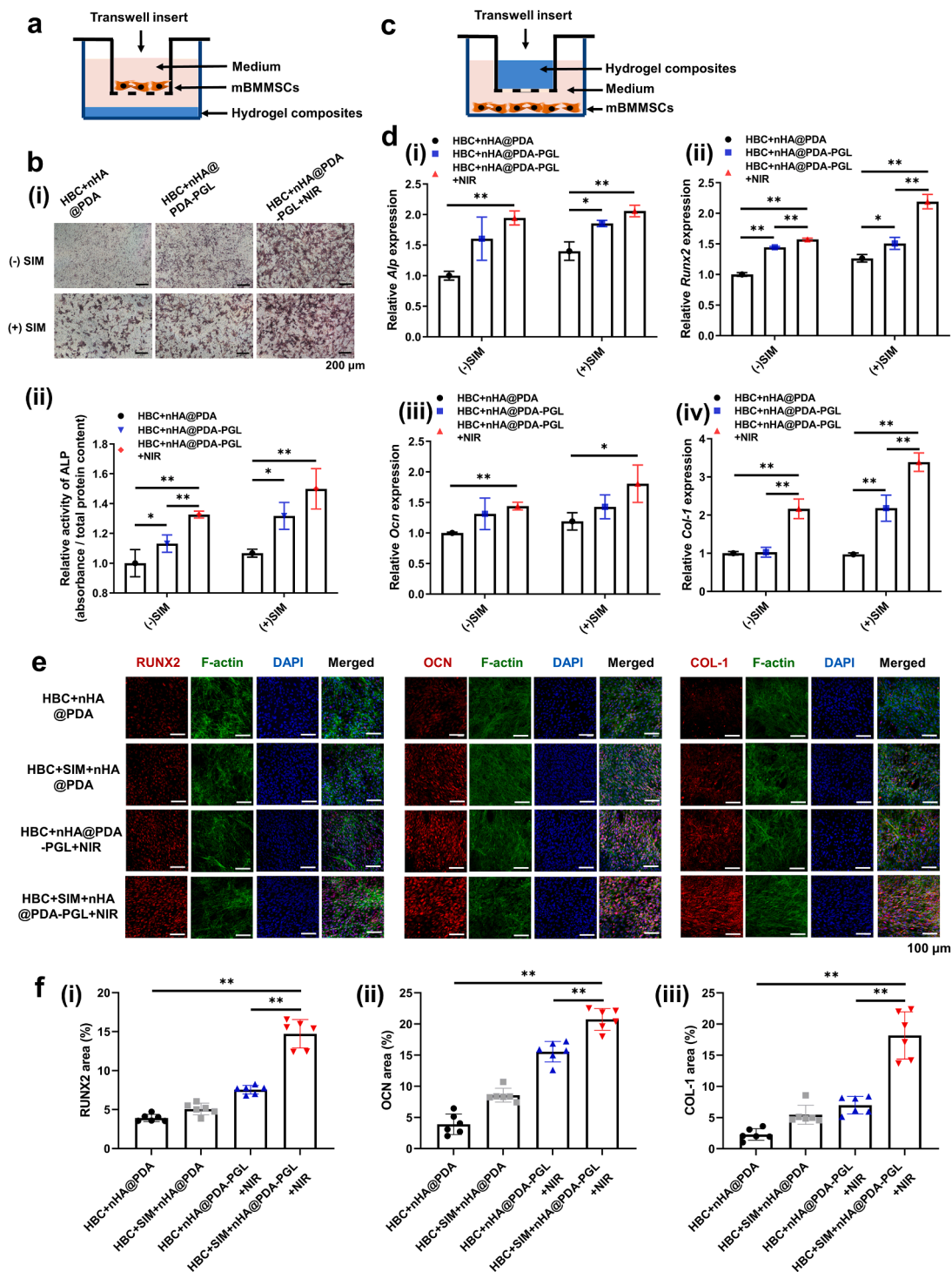


Fig. 6. Evaluation of *in vitro* osteoinductivities of different hydrogel composites. (a) Schematic representation of mBMMSCs cultured with hydrogel composites for migration and *in vitro* osteogenic differentiation evaluation. (b) ALP staining (i) and quantification of the ALP activity (ii) of mBMMSCs cultured with different hydrogel composites via Transwell method. (c) Schematic representation of mBMMSCs cultured with different hydrogel composites. (d) Expression of osteogenic genes including *Alp*, *Runx2*, *Ocn* and *Col-1* of mBMMSCs cultured with different hydrogel composites for 7 days. (e) The expressions of osteogenesis-related proteins, such as RUNX2 (3 days), OCN and COL-1 (7 days), of mBMMSCs after cultured with different hydrogel composites. (f) Semi-quantification of (e) (*: $P < 0.05$. **: $P < 0.01$).

days showed the similar increased OCN and COL-1 expression levels of mBMMSCs after co-cultured with hydrogel composite with programmed release of SIM and PGL.

These results indicated that the programmed release of SIM and PGL exhibited a synergistical effect to promote the osteogenic differentiation of mBMMSCs. While mBMMSCs cultured with

HBC+SIM+PGL+nHA@PDA hydrogel, which could release SIM and PGL simultaneously, led to only slightly enhanced osteogenic differentiation comparing to the control group. Considering that osteogenic ability of PGL was concentration-dependent, it was essential to maintain the concentration of PGL within a suitable range. The suitable concentration of PGL controlled via NIR light irradiation will be favorable to

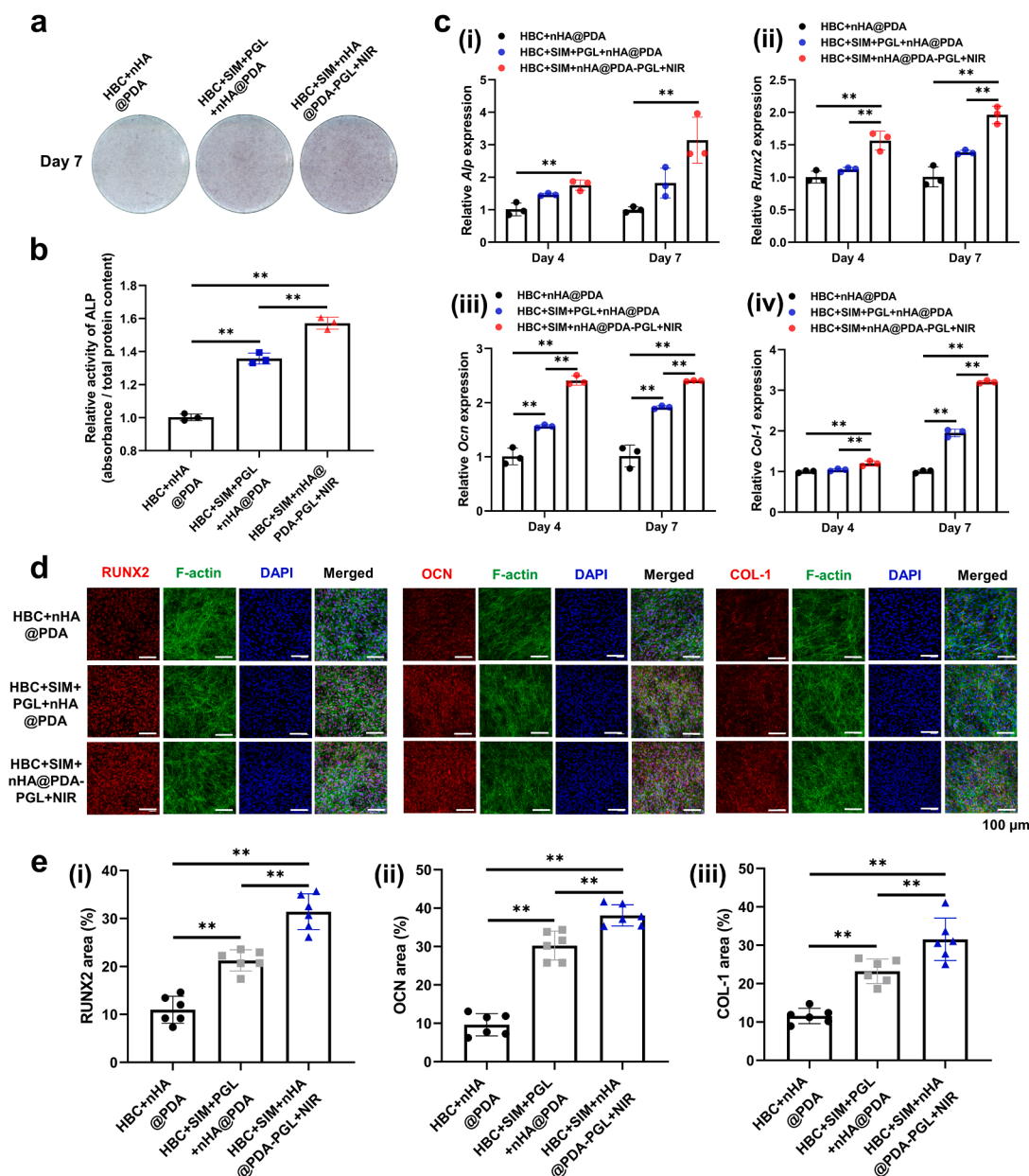


Fig. 7. Evaluation of *in vitro* osteoinductivities of hydrogel composites with programmed release of SIM and PGL. ALP staining (a) and ALP activity (b) of mBMMSCs after culturing with hydrogel composites with different PGL releasing manners for 7 days. (c) Expression of osteogenic genes including *Alp*, *Runx2*, *Ocn* and *Col-1* of mBMMSCs cultured with hydrogel composites with different PGL releasing manners for 4 and 7 days; (d) The expression levels of osteogenesis-related proteins, such as RUNX2 (3 days), OCN and COL-1 (7 days), in mBMMSCs after cultured with hydrogel composites owning different PGL releasing manners. (e) Semi-quantification of (d) (**: $P < 0.01$.)

maximize its osteogenic ability.

3.10. SIM and PGL enhanced *in vivo* bone regeneration

Furthermore, we applied our hydrogel composites to repair the calvarial critical sized defects of C57 mice and evaluate the *in vivo* bone regeneration ($n = 8$ defects per group). From hydrogels injection, NIR light exposure to euthanasia, all mice lived healthy and well. The infrared thermal images of calvarial defect areas implanted with HBC+SIM+nHA@PDA-PGL hydrogel during the NIR light irradiation indicated an efficient photothermal conversion capability of our hydrogel composite (Fig. S5c). The local temperature at the defect sites were controlled under 45 °C during the NIR light irradiation. Eight weeks after hydrogel injection, we evaluated the *in vivo* new bone formation in calvarial bone defects repaired by different hydrogel

composites. The micro-CT images (Fig. S6a) showed that no significant new bone formation in the group without hydrogels (blank), which indicated the defects (diameter: 3 mm) had inability to self-heal. Various degrees of regenerated bone were formed from the edge to the center of the defects in different groups. Furthermore, the ratios of bone volume/tissue volume (BV/TV, %) of different groups were evaluated (Fig. S6b). There was no significant difference in BV/TV of the HBC group and HBC+nHA@PDA group compared to the blank group. The BV/TV value in HBC+SIM+nHA@PDA-PGL+NIR group with programmed released SIM and PGL was highest (39.38%) and significantly higher than HBC+SIM+nHA@PDA group (20.84%) and HBC+nHA@PDA-PGL+NIR group (24.23%) respectively ($P < 0.01$), indicating that the programmed released SIM and PGL played synergistical roles on osteogenesis. The HBC+SIM+nHA@PDA-PGL+NIR group with the controllable release of PGL also performed better osteogenesis capability compared with the

group without NIR light irradiation (HBC+SIM+nHA@PDA-PGL, 30.78%) ($P < 0.05$). In addition, the quality of new bone formation also was observed via histological evaluation (Fig. S6c). The defects treated with HBC+SIM+nHA@PDA-PGL + NIR was occupied with the most obvious bone-like tissue connected the edges, while the blank and HBC groups presented very limited bone tissue and very thin soft tissue covering the defects. Meanwhile, a few residues of hydrogel composites were stained in red and could be found in the defect areas, which was more obvious in Masson staining.

3.11. Augmenting bone formation by programmed release of SIM and PGL

Next, we reasoned that concentration and timeline of small molecules' release should be aligned with the natural healing cascade of bone, in which SIM firstly enhanced the stem cell migration and PGL induce their osteogenic differentiation of the migrated cells. Therefore, we further evaluated the influence of different releasing manners of SIM and PGL on *in vivo* bone regeneration ($n = 10$ defects per group). As shown in Fig. 8a, calvarial samples were obtained at week 12 after the

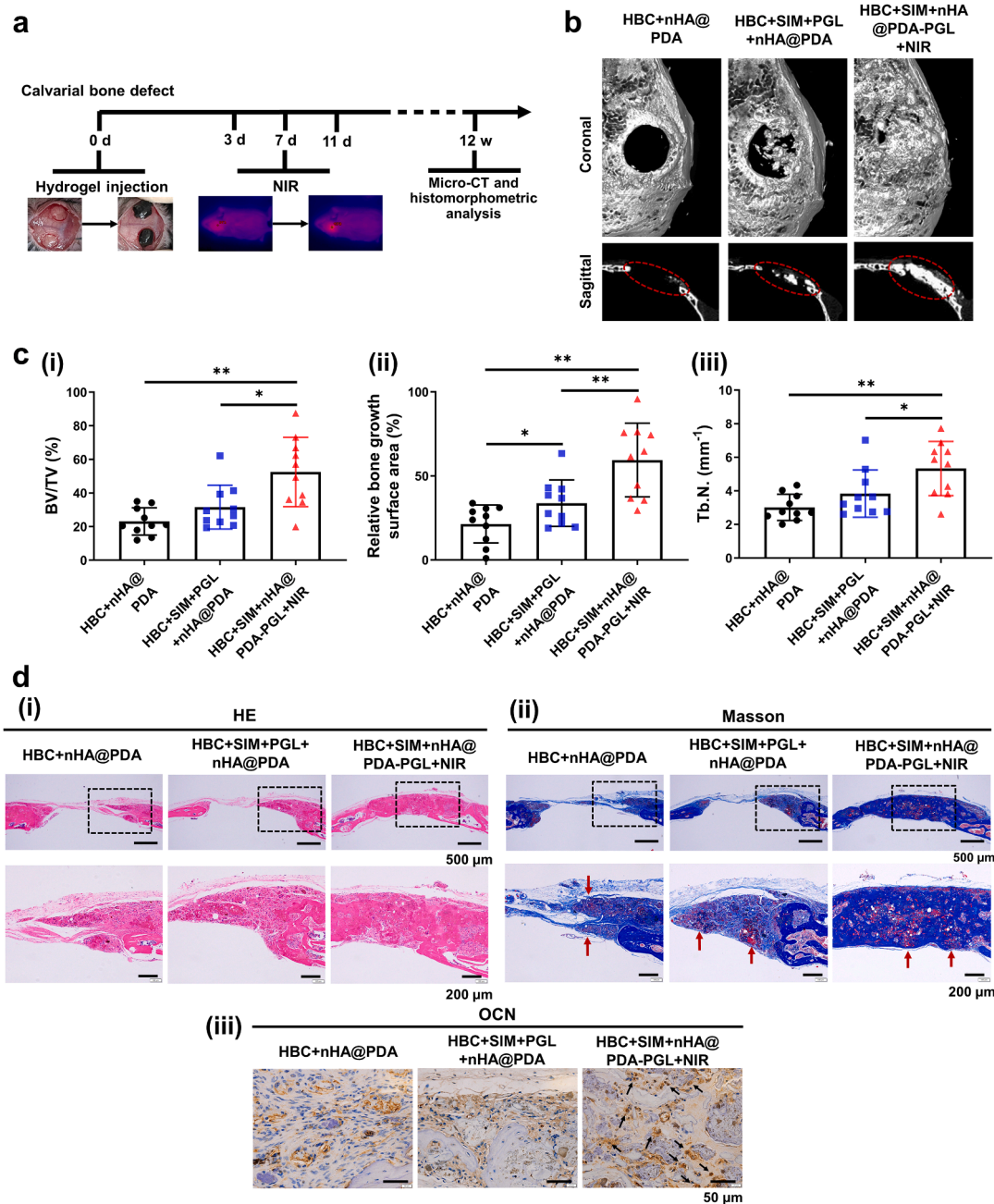


Fig. 8. Evaluation of *in vivo* bone regeneration in groups with different releasing manner of SIM and PGL. (a) Schematic diagram: the 6-week-old C57 mice underwent calvarial defect surgery with the hydrogel composites injected into the defect areas. On the 3rd, 7th and 11th day after surgery, the mice in the NIR light-controlled group treated with 808 nm light irradiation. The calvarial tissues were harvested after 12 weeks for microcomputed tomography (micro-CT) and histomorphometric analysis. (b) Micro-CT images of calvarial bone defects treated with different hydrogel composites, 12 weeks postsurgery. (c) Quantitative comparison of relative bone growth surface area, bone volume/tissue volume (BV/TV, %) and trabecular number (Tb.N., mm⁻¹) between different groups ($n = 10$ defects per group, *: $P < 0.05$, **: $P < 0.01$). (d) Histological analysis of regeneration new bone in defect areas assessed by HE staining, Masson staining as well as immunohistochemical staining for the osteogenic marker OCN (red arrowheads: residues of hydrogel composites; black arrowheads: OCN positive cells).

operation for 3D micro-CT and histomorphometric analysis. Plenty of bone-like tissues covering the defects in the programmed release group (repaired with HBC+SIM+nHA@PDA-PGL hydrogel with NIR light irradiation to control the release of PGL) could be observed in Fig. 8b. The value of bone volume/tissue volume (BV/TV, %) in the programmed release group was significantly elevated to about $52.54 \pm 20.63\%$, while was limited at $23.09 \pm 8.10\%$ in the control group (repaired with HBC+nHA@PDA) (Fig. 8c). It's worth noting that the BV/TV value in group repaired with HBC+SIM+PGL+nHA@PDA hydrogel only increased to $31.59 \pm 13.03\%$, indicating that simultaneous burst release of SIM and PGL at the beginning of bone repair could not promote new bone formation effectively. Moreover, the relative bone growth surface

area (%) and trabecular number (Tb.N., mm^{-1}) increased to 59.46% and 5.33 mm^{-1} for the programmed release group, considerably higher compared with that of the control group (21.41% and 3.02) or the simultaneous release group (33.77% and 3.84), which indicated that the HBC+SIM+nHA@PDA-PGL+NIR group with the programmed release of SIM and PGL possessed the best bone integration ability. The *in vivo* bone regeneration demonstrated that the releasing manner and timing of PGL were important to optimize its therapeutic effect for bone repair, and the programmed released SIM and PGL played synergistic effects for bone regeneration.

Histological analysis of regeneration new bone in defect areas was also performed via HE and Masson staining. As shown in Fig. 8d,

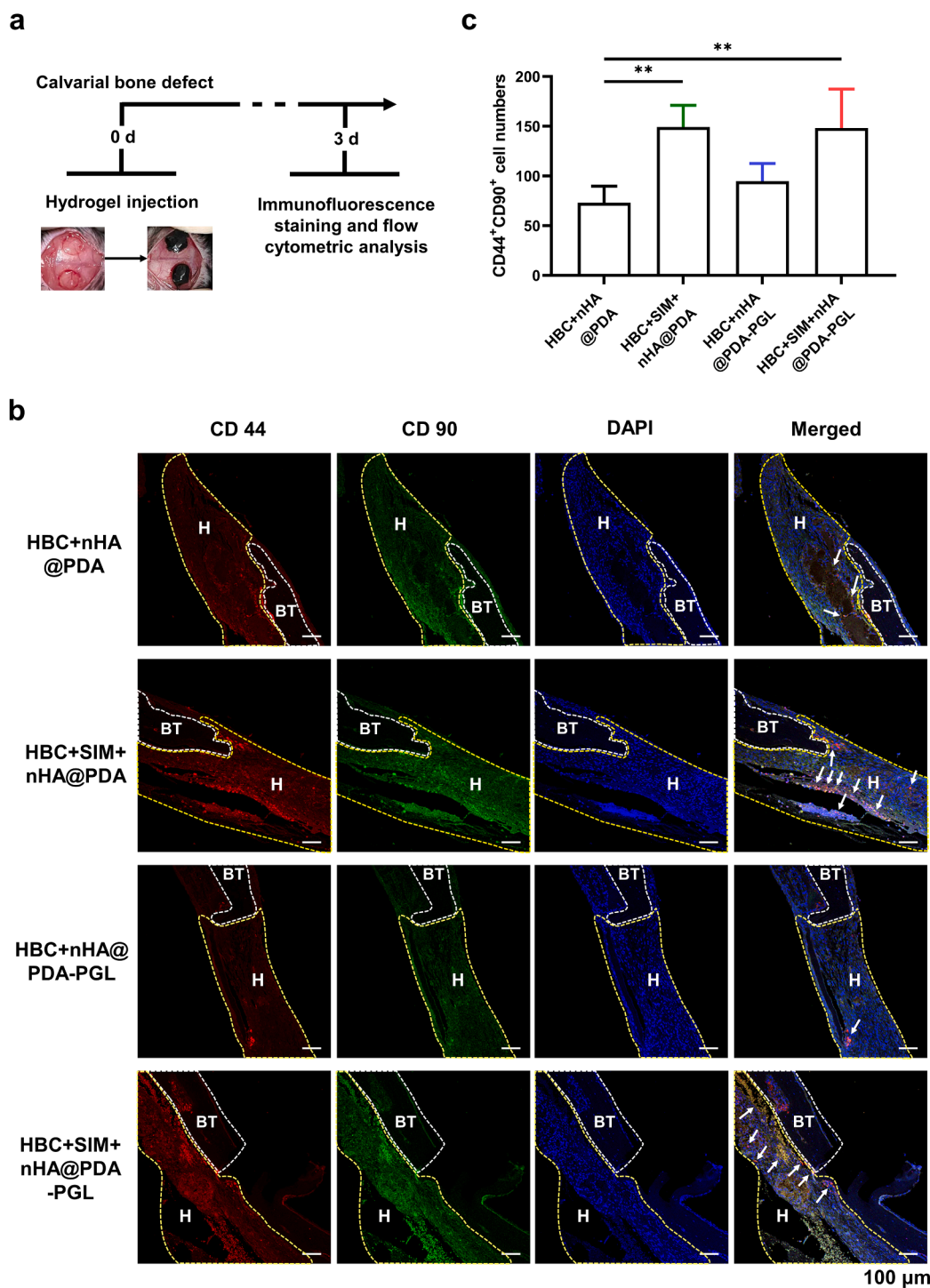


Fig. 9. MSC recruitment ability of the hydrogel composites in calvarial defect areas. (a) Schematic diagram: the 6-week-old C57 mice underwent calvarial defect surgery with the hydrogel composites injected into the defect area ($n = 3$ mice per group). The tissues in defect area were harvested on day 3 for immunofluorescence staining and flow cytometric analysis. (b) The harvested tissues were co-stained with CD44 (red), CD90 (green) and cell nuclei (blue). The white box areas represent the calvarial bone tissue. The yellow box areas represent hydrogel composites as well as the tissue around hydrogels. The white arrows pointed out several CD44⁺CD90⁺ cells. BT: bone tissues, H: hydrogels. (c) Quantification of the CD44⁺CD90⁺ cells in different hydrogel composites via using Image J software ($n = 6$ defects per group).

different degrees of new bone formation were observed in three groups. In particular, the defects in the programmed release group were obviously occupied with newly formed bone, the thickness of which was nearly same as that of original bone. The simultaneous release group present less new bone formation only on the edges of the defects. The residues of hydrogel composites also could be observed in three groups after 12 weeks of implantation. Images of immunohistochemical staining for the osteogenic marker OCN also showed that the dark-brown granules were much more in programmed release group, indicating that higher number of OCN positive cells were observed. However, the simultaneous release of SIM and PGL may restrict the *in vivo* performance of HBC+SIM+PGL+nHA@PDA hydrogel.

Meanwhile, the histology of hearts, livers, spleens, and kidneys showed no abnormalities or pathological changes in all experimental groups compared with the mice without hydrogel injection (Fig. S7), suggesting that our hydrogel composites cannot induce any obvious systemic reaction, and hence can be used *in vivo* with good biocompatibility. The *in vivo* biodegradation behaviors of the hydrogel composites were also evaluated via subcutaneous injection into the dorsal areas of nude mice. As shown in the macroscopical photographs (Fig. S8), part of hydrogels was degraded *in vivo* and the volume of hydrogels was obviously reduced after 4 weeks and 8 weeks of observation. The HE staining images showed that the structure of hydrogel tended to be incomplete and more fibrous tissue could be observed around and inside the hydrogel composite. In addition, there was no obvious inflammatory response or necrosis in all experimental groups.

3.12. *In vivo* MSC recruitment by the SIM loaded hydrogels

As demonstrated in Fig. 9a, the *in vivo* MSC recruitment conducted by SIM loaded hydrogel composites at calvarial defect areas was studied through immunofluorescence staining after 3 days of hydrogel injection. Classical cell surface markers, CD44 and CD90, were selected as the markers of endogenous MSCs [64]. Confocal images demonstrated that CD44 (red) and CD90 (green) double-positive cells were more concentrated at the defect areas in HBC+SIM+nHA@PDA and HBC+SIM+nHA@PDA-PGL groups (Fig. 9b). As shown in Fig. 9c, the numbers of CD44⁺CD90⁺ cells in SIM-loaded groups were significantly higher than HBC+nHA@PDA group without drugs loading. Similarly, as shown in results of flow cytometric analysis (Fig. 10), after 3 days of implantation, the percentages of CD45⁻TER119⁻CD44⁺CD90⁺ cells in SIM-containing hydrogels groups were significantly higher than that of in HBC+nHA@PDA group. These results suggested that the SIM-containing hydrogel composites could effectively capture and enrich the surrounding MSCs to the defect areas at the early stage of tissue remodeling, which will benefit the further regeneration of damaged bone tissue *in vivo*.

3.13. The epigenetic effects of hydrogel composites

The potential epigenetic effects of PGL-loaded hydrogel composites were subsequently investigated through immunofluorescence staining and ChIP assay. Two representative groups, HBC + nHA@PDA group (without PGL) and HBC+nHA@PDA-PGL+NIR group (with NIR light-controlled released PGL and without the influence of SIM), were chosen for the analysis of epigenetic mechanism. The immunofluorescence images of mBMMSCs in HBC+nHA@PDA-PGL+NIR group exhibited much higher levels of methylation in H3K4, especially the mono-methylation and di-methylation of H3K4 (H3K4me1, H3K4me2) after 7 days of culture (Fig. 11a, b). The similar expression levels of methylation of H3K4 were observed in calvarial defect areas repaired with hydrogel composites for 2 weeks (Fig. S9). The group with the controllable release of PGL induced much higher levels of H3K4me1 and H3K4me2 in defect areas compared with the group without the loading of PGL.

Furthermore, the results of ChIP assay in Fig. 11c demonstrated enhanced levels of H3K4me2 at the promoter regions of osteogenesis-related genes, such as *Runx2* and *Ocn*. Compared with the HBC+nHA@PDA group, the expression level of H3K4me2 in HBC+nHA@PDA-PGL+NIR group was increased hugely at the *Runx2* as well as *Ocn* promoter regions. Simultaneously, the histone H3 level was considered as the positive control, and there was no much difference of H3 levels between the HBC+nHA@PDA and HBC+nHA@PDA-PGL+NIR groups. Moreover, the negative control IgG was detected to exclude the possibility of false positive results.

These results demonstrated that hydrogel composite with the controlled release of PGL could promote the osteogenic differentiation of mBMMSCs by enhancing the di-methylation level of H3K4, giving a better understanding of the epigenetic mechanism of how PGL-loaded hydrogel composites modulate the stem cells' fates and enhance bone regeneration.

4. Discussion

Bone tissue regeneration is a well-orchestrated process and the controlled release of chemotactic and osteogenic biomolecules could efficiently enhance bone tissue regeneration [40,65–67]. Especially, it has been reported that the osteoinductive biomolecules were maximized beneficial when applied after the formation of a stable hematoma and the recruitment of the osteoprogenitor cells [68–70]. However, the current delivery systems mostly regulate the release timeline of biomolecules via encapsulating them within multi-material-based or multi-layer-based structures, which is still heavily dependent on the degradation rates, initial porosity as well as processing conditions of matrix [11,13,40]. The therapeutic concentrations and time points of

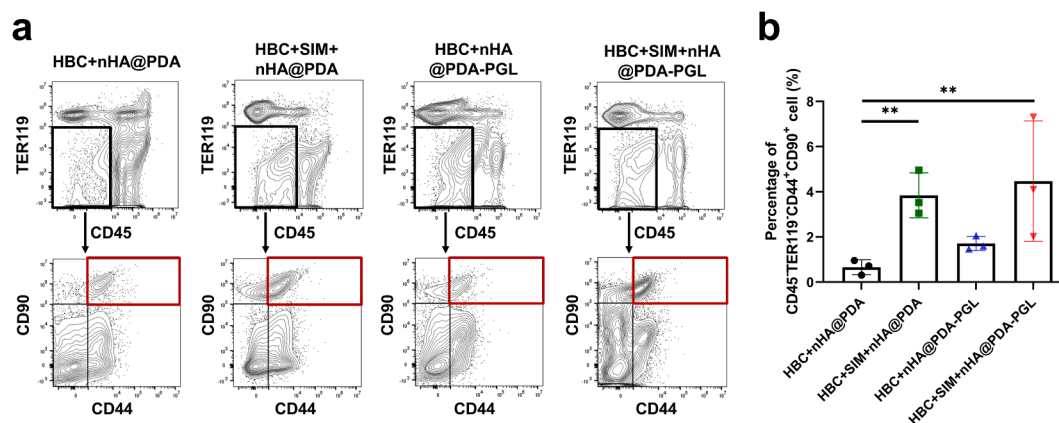


Fig. 10. (a) Representative flow cytometric profiles of sort gates of CD45-negative, TER119-negative, CD44-positive, and CD90-positive cells. (b) Quantitative histogram of the percentages of recruited CD45⁻TER119⁻CD44⁺CD90⁺ cells (n = 3 mice per group). (*: $P < 0.05$. **: $P < 0.01$.)

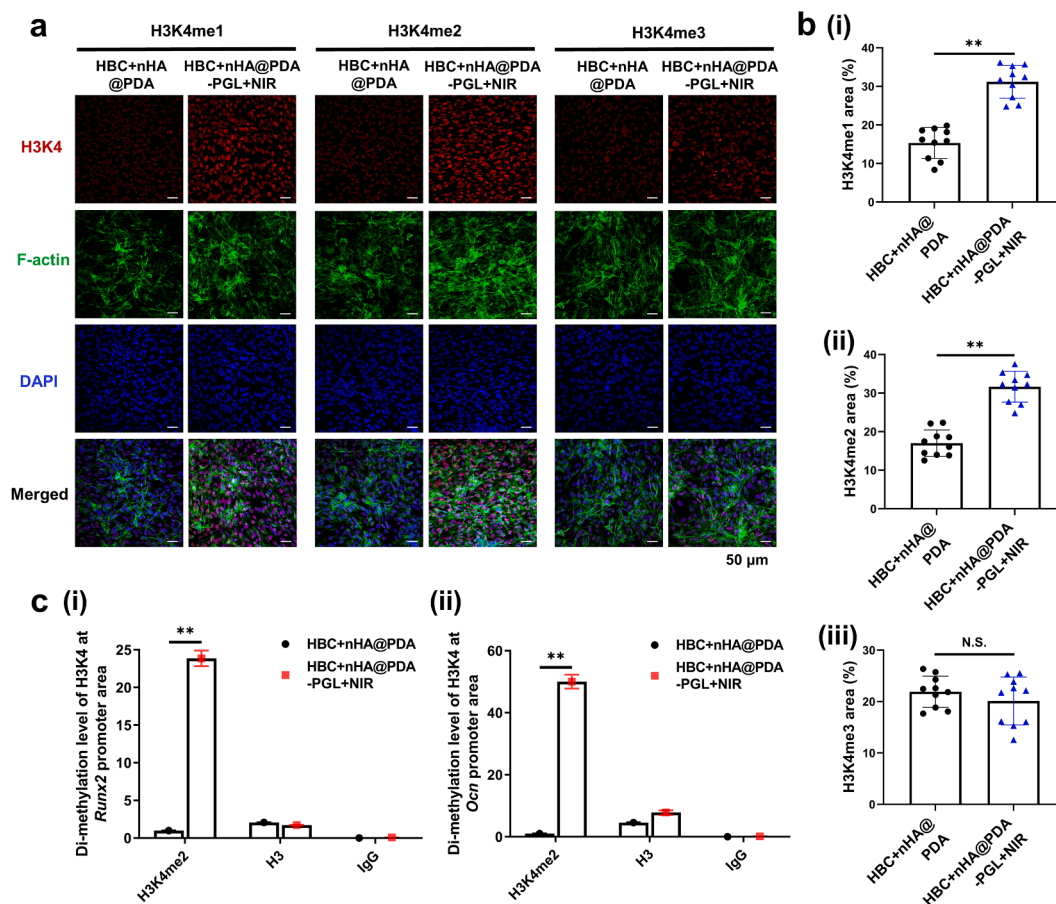


Fig. 11. Epigenetic regulation of PGL-loaded hydrogel composites on mBMMSCs. (a) Immunofluorescent staining for methylation of H3K4 in mBMMSCs cultured with HBC+nHA@PDA and HBC+nHA@PDA-PGL+NIR hydrogels for 7 days. The methylation levels of H3K4 were shown in red, the cytoskeletons were in green and nuclei were in blue. (b) Semi-quantification of (a). (c) ChIP assay of di-methylation level of H3K4 at the promoter area of osteogenic *Runx2* and *Ocn* at 7 days after cultured with hydrogel composites. (**: $P < 0.01$.)

biomolecules are still difficult to control. Here, we designed a programmed delivery system by combining thermo-responsive HBC hydrogel with the NIR light-responsive nHA@PDA to enhance bone tissue regeneration via regulating the on-demand release of two bioactive small molecules. This programmed delivery system performed a burst release of SIM to reach its therapeutic concentration rapidly and enhance the recruitment of MSCs at the beginning of bone repair. Subsequently, a flexible release of PGL was obtained under the control of NIR light to regulate the therapeutic concentration and time point of drug, thereby facilitating the osteogenic differentiation of recruited MSCs via a stable and safe epigenetic mechanism. By programming the release of two small molecules, our delivery system could well orchestrate the process of bone healing, providing a unique and efficient strategy for bone tissue regeneration.

The utilization of two small molecular drugs in our programmed delivery system has explored a novel option for bone tissue engineering. Compared with the traditional chemokines (such as stromal cell derived factor-1, interleukin-8) and osteogenic proteins or peptides (such as bone morphogenetic proteins), which have short half-life and slow tissue penetration, these small molecular drugs are cheaper, stabler, and more accessible, making them more suitable for the responsive drug delivery systems, especially under the NIR light irradiation [41]. Besides, both SIM and PGL have been approved by the U.S. Food and Drug Administration (FDA) and achieved commercial success [71,72]. The pharmacokinetics and safety considerations of drugs also have been evaluated [73,74], which made their translation and further application in the field of bone tissue engineering possible and easier. Our results demonstrated that a low concentration of SIM could perform an efficient

chemotactic capacity to recruit MSCs both *in vitro* and *in vivo* (Fig. 5, Fig. 9 & Fig. 10). The programmed delivery of SIM and PGL have exhibited synergistic effect on osteogenic differentiation of mBMMSCs (Fig. 6) and *in vivo* bone regeneration (Fig. S6). Especially, the epigenetic mechanism involved in the PGL loaded hydrogel composites was also investigated (Fig. 11). The epigenetic regulation could influence the expression of genes via histone modification, DNA methylation, as well as RNA interference, and play essential roles in cancer therapy and bone homeostasis [75,76]. Our previous studies have reported that PGL enables to effectively inhibit the activity of demethylase lysine-specific demethylase 1 (LSD1) and rescue the osteogenic differentiation ability of mBMMSCs under osteoporotic conditions [45,46]. By controlling the release of PGL, our hydrogel composite significantly increased the demethylation level of histone at the promoter regions of osteogenesis-related genes (*Runx2* and *Ocn*) in mBMMSCs. Compared with addition of osteogenic factors or the expression of exogenous genes, this epigenetic regulation was stabler and more potentially heritable without altering the sequence of DNA [77,78]. With a deeper understanding of epigenetic regulation as well as epigenetic therapy, our study provided an efficient alternative for bone tissue engineering via controlling the release of similar epigenetic small molecules, providing more possibilities for further clinical transformation.

To program the therapeutic concentration and time points of SIM and PGL in bone tissue regeneration, a well-designed stimuli-responsive hydrogel composite was utilized as the drugs carrier in this study. It has been demonstrated that the dynamic hydrogels possess unique extracellular matrix-like, three-dimensional networks, which enable to deliver multiple kinds of therapeutic agents and provide local rigid cell

anchorage sites for various cellular events [79–85]. The tunable stiff network structures of hydrogels could support the infiltration of endogenous stem cells and modulate their mechanosensing capacity, thereby facilitating the osteogenic differentiation of cells and enhancing the *in vivo* bone tissue regeneration [86–88]. Thereafter, the thermo-responsive HBC hydrogel with reversible “sol–gel” transformation capacity (Fig. 3a), unique thixotropic property (Fig. S3), as well as suitable injectability (Fig. 8a) was successfully prepared, which could serve as a suitable and stable carrier for SIM and PGL loaded nanoparticles [38,89–91]. A fast and efficient release of SIM could be observed (Fig. 4a) at the beginning of releasing to reach its therapeutic concentration rapidly within a short time period, after which a slow and decreased release of SIM still existed for a long time. The SIM loaded in hydrogel composite mainly released via physical diffusion and accompanied with the biodegradation of hydrogel [92]. The hydrophobicity of SIM may restrict its full release and almost 56% of SIM could be finally released after 28 days of observation. In addition, this hydrogel composite with initial sol phase could flow and fill the 3 mm-sized calvarial bone defect areas and transform into the immobile gel under the physiological environment without using the cytotoxic initiators or cross-linking agents (Fig. 8a), thereby facilitating its further application in repair of irregular shaped or deep bone defects via a minimally invasive manner [79–84].

In addition, the NIR light-responsive drug delivery systems have exhibited enormous potential for controllable release of biomolecules at targeted bone tissues [93–95]. On the one hand, the NIR light (700–1350 nm) displays higher tissue penetration depth (≈ 1 –2 cm) and less damages to normal tissues compared with ultraviolet (200–400 nm) or visible (400–700 nm) light due to its minimum refraction and attenuation by endogenous biomolecules and chromophores (e.g., water, blood, and melanin), making it more suitable to apply in bone tissue engineering [96–99]. On the other hand, the NIR light-triggered release of biomolecules could be successfully activated via photothermal (generation of heat) and photodynamic (production of reactive oxygen species) mechanisms [100]. The photosensitive agents with high energy-absorption/conversion capability are needed to ensure its therapeutic efficiency in clinical applications [101,102]. Currently, the NIR light-responsive delivery systems have been applied for the on-demand release of anti-tumor or anti-infection drugs for the treatment of bone cancers, infections, and inflammation, while only a few studies reported their application for bone tissue regeneration [23,103,104]. For example, a heat-activated and dimerizer-dependent transgene expression system incorporated with a NIR light-responsive hydrogel has been designed for the controllable release of bone morphogenetic protein 2 [105]. However, the complexity and limited tenability of delivery system was still restricted in further applications.

Recent studies have demonstrated that the mussel-inspired material, PDA, possesses higher excellent photothermal conversion efficiency compared with many photothermal agents, such as carbon-based nanomaterials, Cu-based nanoparticles, Au-based metal nanoparticles, and organic polymers [28,32]. It also possesses many ideal properties for tissue engineering, such as strong adhesive capacity, good biocompatibility, as well as simple preparation process [28]. The PDA coating with abundant functional groups, such as catechol, amine, and imine, could act as the anchors for multiple kind of biomolecules via π – π stacking, electrostatic adsorption and hydrogen bonding interactions [106–108]. Due to the high photothermal conversion efficiency of PDA under the NIR light irradiation, the above interactions between biomolecules and PDA would become looser and the release of biomolecules could markedly increase accompanied with the rise of temperature [109]. Thereafter, the NIR light-responsive nHA@PDA nanoparticles have been designed to control the on-demand release of osteogenic small molecule PGL in this study. Unlike the PGL being simply dissolved in hydrogel composite which exhibited the concentration gradient-dependent drug diffusion, our HBC + nHA@PDA-PGL hydrogel exhibited a more controllable NIR-triggered “off–on” release of PGL (Fig. 4b). This

flexible NIR light-triggered release manner may be beneficial to prolong the accumulation of PGL followed by the therapeutic effects of SIM, maximizing their synergistical effects to promote the osteogenic differentiation of stem cells (Fig. 7) and enhance the new bone formation at the calvarial bone defect sites (Fig. 8). Meanwhile, it should be noticed that hyperthermia (over 50 °C), resulted from the photothermal effect of NIR light, can potentially induce cell damage and necrosis both in tumor and healthy regions [110–112]. In this study, we refined the irradiation parameters of NIR light irradiation and maintained the tissue temperature under 45 °C to avoid over-heating of local tissue, making it suitable for bone tissue regeneration.

In a word, our programmed delivery system successfully enhanced bone tissue regeneration via programming the on-demand release of both chemotactic SIM and osteogenic PGL. The novel usage of classical drugs, SIM and PGL, not only reduced the cost of manufacturing, but also was easy for clinical transformation based on the known pharmacological effects and existing safety evaluation of drugs. However, a few challenges should be overcome when broadening its application for the on-demand delivery of other biomolecules. Firstly, the HBC hydrogel performed a burst and rapid release profile of SIM, which may restrict its further applications for the delivery of other biomolecules with a sustained and long-time release. What's more, the NIR light-triggered drug carrier had great advantages for the on-demand release of small molecule drugs, while it may not be suitable for the delivery of bioactive proteins and peptides with low stability and short half-lives. More modifications should be made to optimize our programmed delivery system and extend its future applications for regenerative medicine and bone tissue engineering.

5. Conclusion

In this study, our programmed delivery system could perform an on-demand release of two small molecules, in which an initial and rapid release of SIM was performed at the early stage of bone regeneration followed by a flexible NIR light-controlled release of PGL. This programmed delivery system successfully orchestrated the bone tissue regeneration via MSC recruitment and epigenetic modulation, providing great insights into the design of efficient delivery systems for bone tissue engineering and regenerative medicine.

Declaration of Competing Interest

The authors declare that they have no known competing financial interests or personal relationships that could have appeared to influence the work reported in this paper.

Acknowledgements

This study was supported by grants from the Beijing Natural Science Foundation (7192228) and from the Young Elite Scientist Sponsorship Program by CAST (2015QNRC001).

Appendix A. Supplementary data

Supplementary data to this article can be found online at <https://doi.org/10.1016/j.cej.2022.135518>.

References

- [1] S. Facca, C. Cortez, C. Mendoza-Palomares, N. Messadeq, A. Dierich, A. P. Johnston, D. Mainard, J.C. Voegel, F. Caruso, N. Benkirane-Jessel, Active multilayered capsules for *in vivo* bone formation, *Proc. Natl. Acad. Sci. U. S. A.* 107 (8) (2010) 3406–3411, <https://doi.org/10.1073/pnas.0908531107>.
- [2] D. Taylor, J.G. Hazenberg, T.C. Lee, Living with cracks: Damage and repair in human bone, *Nature Mater.* 6 (4) (2007) 263–268, <https://doi.org/10.1038/nmat1866>.

- [3] Y. Liu, J. Lim, S.H. Teoh, Review: development of clinically relevant scaffolds for vascularised bone tissue engineering, *Biotechnol. Adv.* 31 (5) (2013) 688–705, <https://doi.org/10.1016/j.biotechadv.2012.10.003>.
- [4] S. Pacelli, S. Basu, J. Whitlow, A. Chakravarti, F. Acosta, A. Varshney, S. Modaresi, C. Berkland, A. Paul, Strategies to develop endogenous stem cell-recruiting bioactive materials for tissue repair and regeneration, *Adv. Drug Deliv. Rev.* 120 (2017) 50–70, <https://doi.org/10.1016/j.addr.2017.07.011>.
- [5] K.D. Hankenson, K. Gagne, M. Shaughnessy, Extracellular signaling molecules to promote fracture healing and bone regeneration, *Adv. Drug Deliv. Rev.* 94 (2015) 3–12, <https://doi.org/10.1016/j.addr.2015.09.008>.
- [6] M. Farokhi, F. Mottaghtalab, M.A. Shokrgozar, K.-L. Ou, C. Mao, H. Hosseinkhani, Importance of dual delivery systems for bone tissue engineering, *J. Control. Release* 225 (2016) 152–216, <https://doi.org/10.1016/j.jconrel.2016.01.033>.
- [7] T. Sun, C. Meng, Q. Ding, K. Yu, X. Zhang, W. Zhang, W. Tian, Q. Zhang, X. Guo, B. Wu, Z. Xiong, *In situ* bone regeneration with sequential delivery of aptamer and BMP2 from an ECM-based scaffold fabricated by cryogenic free-form extrusion, *Bioact. Mater.* 6 (11) (2021) 4163–4175, <https://doi.org/10.1016/j.bioactmat.2021.04.013>.
- [8] P.S. Lienemann, Q. Vallmajo-Martin, P. Papageorgiou, U. Blache, S. Metzger, A.-S. Kiveliö, V. Milleret, A. Sala, S. Hoehnel, A. Roch, R. Reuten, M. Koch, O. Naveiras, F.E. Weber, W. Weber, M.P. Lutolf, M. Ehrbar, Smart hydrogels for the augmentation of bone regeneration by endogenous mesenchymal progenitor cell recruitment, *Adv. Sci. (Weinh)* 7 (7) (2020) 1903395, <https://doi.org/10.1002/advs.201903395>.
- [9] H. Li, H. Wang, J. Pan, J. Li, K. Zhang, W. Duan, H. Liang, K. Chen, D. Geng, Q. Shi, H. Yang, B. Li, H. Chen, Nanoscaled bionic periosteum orchestrating the osteogenic microenvironment for sequential bone regeneration, *ACS Appl. Mater. Interfaces* 12 (33) (2020) 36823–36836, <https://doi.org/10.1021/acsmi.0c06906>.
- [10] J.E. Samorezov, E. Alsborg, Spatial regulation of controlled bioactive factor delivery for bone tissue engineering, *Adv. Drug Deliv. Rev.* 84 (2015) 45–67, <https://doi.org/10.1016/j.addr.2014.11.018>.
- [11] Y.-H. Kim, Y. Tabata, Dual-controlled release system of drugs for bone regeneration, *Adv. Drug Deliv. Rev.* 94 (2015) 28–40, <https://doi.org/10.1016/j.addr.2015.06.003>.
- [12] L. Frapin, J. Clouet, V. Delplace, M. Fusellier, J. Guicheux, C. Le Visage, Lessons learned from intervertebral disc pathophysiology to guide rational design of sequential delivery systems for therapeutic biological factors, *Adv. Drug Deliv. Rev.* 149–150 (2019) 49–71, <https://doi.org/10.1016/j.addr.2019.08.007>.
- [13] E.A. Bayer, R. Gottardi, M.V. Fedorchak, S.R. Little, The scope and sequence of growth factor delivery for vascularized bone tissue regeneration, *J. Control. Release* 219 (2015) 129–140, <https://doi.org/10.1016/j.jconrel.2015.08.004>.
- [14] A.M. Vargason, A.C. Anselmo, S. Mitragotri, The evolution of commercial drug delivery technologies, *Nat. Biomed. Eng.* 5 (9) (2021) 951–967, <https://doi.org/10.1038/s41551-021-00698-w>.
- [15] S. Saravanan, S. Vimalraj, P. Thanikaivelan, S. Banudevi, G. Manivasagam, A review on injectable chitosan/beta glycerophosphate hydrogels for bone tissue regeneration, *Int. J. Biol. Macromol.* 121 (2019) 38–54, <https://doi.org/10.1016/j.ijbiomac.2018.10.014>.
- [16] F. Qu, J.L. Holloway, J.L. Esterhai, J.A. Burdick, R.L. Mauck, Programmed biomolecule delivery to enable and direct cell migration for connective tissue repair, *Nat. Commun.* 8 (1) (2017) 1780, <http://doi:10.1038/s41467-017-01955-w>.
- [17] Z. Liu, X. Chen, Z. Zhang, X. Zhang, L. Saunders, Y. Zhou, P.X. Ma, Nanofibrous spongy microspheres to distinctly release miRNA and growth factors to enrich regulatory T cells and rescue periodontal bone loss, *ACS nano* 12 (10) (2018) 9785–9799, <http://doi:10.1021/acsnano.7b08976>.
- [18] W. Zhang, C. Ling, A. Zhang, H. Liu, Y. Jiang, X. Li, R. Sheng, Q. Yao, J. Chen, An all-silk-derived functional nanosphere matrix for sequential biomolecule delivery and *in situ* osteochondral regeneration, *Bioact. Mater.* 5 (4) (2020) 832–843, <https://doi.org/10.1016/j.bioactmat.2020.05.003>.
- [19] Y. Wang, Programmable hydrogels, *Biomaterials* 178 (2018) 663–680, <https://doi.org/10.1016/j.biomaterials.2018.03.008>.
- [20] J. Wu, K. Zheng, X. Huang, J. Liu, H. Liu, A.R. Boccaccini, Y. Wan, X. Guo, Z. Shao, Thermally triggered injectable chitosan/silk fibroin/bioactive glass nanoparticle hydrogels for *in-situ* bone formation in rat calvarial bone defects, *Acta Biomater.* 91 (2019) 60–71, <https://doi.org/10.1016/j.actbio.2019.04.023>.
- [21] X. Xu, Z. Gu, X.i. Chen, C.e. Shi, C. Liu, M. Liu, L. Wang, M. Sun, K. Zhang, Q. Liu, Y. Shen, C. Lin, B. Yang, H. Sun, An injectable and thermosensitive hydrogel: Promoting periodontal regeneration by controlled-release of aspirin and erythropoietin, *Acta Biomater.* 86 (2019) 235–246, <https://doi.org/10.1016/j.actbio.2019.01.001>.
- [22] H. Ding, B. Li, Z. Liu, G. Liu, S. Pu, Y. Feng, D. Jia, Y.u. Zhou, Decoupled pH- and Thermo-Responsive Injectable Chitosan/PNIPAM Hydrogel via Thiol-Ene Click Chemistry for Potential Applications in Tissue Engineering, *Adv. Healthcare Mater.* 9 (14) (2020) 2000454, <https://doi.org/10.1002/adhm.v.9.1410.1002/adhm.202000454>.
- [23] Y. Xue, W. Niu, M. Wang, M. Chen, Y. Guo, B. Lei, Engineering a biodegradable multifunctional antibacterial bioactive nanosystem for enhancing tumor photothermo-chemotherapy and bone regeneration, *ACS nano* 14 (1) (2020) 442–453, <http://doi:10.1021/acsnano.9b06145>.
- [24] Y. Zhao, C. Wei, X. Chen, J. Liu, Q. Yu, Y. Liu, J. Liu, Drug delivery system based on near-infrared light-responsive molybdenum disulfide nanosheets controls the high-efficiency release of dexamethasone to inhibit inflammation and treat osteoarthritis, *ACS Appl. Mater. Interfaces* 11 (12) (2019) 11587–11601, <http://doi:10.1021/acsmi.8b20372>.
- [25] C. Yin, Q. Zhao, W.u. Li, Z. Zhao, J. Wang, T. Deng, P. Zhang, K. Shen, Z. Li, Y. Zhang, Biomimetic anti-inflammatory nano-capsule serves as a cytokine blocker and M2 polarization inducer for bone tissue repair, *Acta Biomater.* 102 (2020) 416–426, <https://doi.org/10.1016/j.actbio.2019.11.025>.
- [26] W. Sun, K. Ge, Y. Jin, Y.u. Han, H. Zhang, G. Zhou, X. Yang, D. Liu, H. Liu, X.-J. Liang, J. Zhang, Bone-targeted nanopatform combining zoledronate and photothermal therapy to treat breast cancer bone metastasis, *ACS Nano* 13 (7) (2019) 7556–7567, <https://doi.org/10.1021/acsnano.9b0009710.1021/acsnano.9b00097.s001>.
- [27] Z. Wan, P. Zhang, L. Lv, Y. Zhou, NIR light-assisted phototherapies for bone-related diseases and bone tissue regeneration: A systematic review, *Theranostics* 10 (25) (2020) 11837–11861, <https://doi.org/10.7150/thno.49784>.
- [28] W. Cheng, X. Zeng, H. Chen, Z. Li, W. Zeng, L. Mei, Y. Zhao, Versatile polydopamine platforms: Synthesis and promising applications for surface modification and advanced nanomedicine, *ACS Nano* 13 (8) (2019) 8537–8565, <https://doi.org/10.1021/acsnano.9b04436>.
- [29] Y. Ding, M. Floren, W. Tan, Mussel-inspired polydopamine for bio-surface functionalization, *Biosurf. Biotribol.* 2 (4) (2016) 121–136, <https://doi.org/10.1016/j.bsbt.2016.11.001>.
- [30] X. Wang, J. Zhang, Y. Wang, C. Wang, J. Xiao, Q. Zhang, Y. Cheng, Multi-responsive photothermal-chemotherapy with drug-loaded melanin-like nanoparticles for synergetic tumor ablation, *Biomaterials* 81 (2016) 114–124, <https://doi.org/10.1016/j.biomaterials.2015.11.037>.
- [31] F. Liu, X. He, Z. Lei, L. Liu, J. Zhang, H. You, H. Zhang, Z. Wang, Facile preparation of doxorubicin-loaded upconversion/polydopamine nanopatforms for simultaneous *in vivo* multimodality imaging and chemophotothermal synergistic therapy, *Adv. Healthc. Mater.* 4 (4) (2015) 559–568, <http://doi:10.1002/adhm.201400676>.
- [32] Y. Liu, K. Ai, J. Liu, M. Deng, Y. He, L. Lu, Dopamine-melanin colloidal nanospheres: an efficient near-infrared photothermal therapeutic agent for *in vivo* cancer therapy, *Adv. Mater.* 25 (9) (2013) 1353–1359, <http://doi:10.1002/adma.201204683>.
- [33] K. Zhang, Z. Jia, B. Yang, Q. Feng, X. Xu, W. Yuan, X. Li, X. Chen, L.i. Duan, D. Wang, L. Bian, Adaptable Hydrogels Mediate Cofactor-Assisted Activation of Biomarker-Responsive Drug Delivery via Positive Feedback for Enhanced Tissue Regeneration, *Adv. Sci.* 5 (12) (2018) 1800875, <https://doi.org/10.1002/advs.v.5.1210.1002/advs.201800875>.
- [34] M. Lee, Z. Cui, S. Kim, J. Baljon, B. Wu, T. Aghaloo, Microporous methacrylated glycol chitosan-montmorillonite nanocomposite hydrogel for bone tissue engineering, *Nat. Commun.* 10 (2019) 1–10, <https://doi.org/10.1038/s41467-019-11511-3>.
- [35] A. Sivashanmugam, P. Charoenlarp, S. Deepthi, A. Rajendran, S.V. Nair, S. Iseki, R. Jayakumar, Injectable shear-thinning CaSO₄/FGF-18-incorporated chitin-PLGA hydrogel enhances bone regeneration in mice cranial bone defect model, *ACS Appl. Mater. Interfaces* 9(49) (2017) 42639–42652, <http://doi:10.1021/acsmi.7b15845>.
- [36] S. Graham, P.F. Marina, A. Blencowe, Thermoresponsive polysaccharides and their thermoreversible physical hydrogel networks, *Carbohydr. Polym.* 207 (2019) 143–159, <https://doi.org/10.1016/j.carbpol.2018.11.053>.
- [37] Z. Bao, P. Gao, G. Xia, Z. Wang, M. Kong, C. Feng, X. Cheng, Y. Liu, X. Chen, A thermosensitive hydroxybutyl chitosan hydrogel as a potential co-delivery matrix for drugs on keloid inhibition, *J. Mat. Chem. B* 4 (22) (2016) 3936–3944, <https://doi.org/10.1039/c6tb00378h>.
- [38] M. Sun, T. Wang, J. Pang, X. Chen, Y. Liu, Hydroxybutyl chitosan centered biocomposites for potential curative applications: A critical review, *Biomacromolecules* 21 (4) (2020) 1351–1367, <https://doi.org/10.1021/acs.biomac.0c00071>.
- [39] Q. Chen, C. Zheng, Y. Li, S. Bian, H. Pan, X. Zhao, W.W. Lu, Bone targeted delivery of SDF-1 via alendronate functionalized nanoparticles in guiding stem cell migration, *ACS Appl. Mater. Interfaces* 10 (28) (2018) 23700–23710, <http://doi:10.1021/acsmi.8b08606>.
- [40] D. Lin, Y. Chai, Y. Ma, B. Duan, Y. Yuan, C. Liu, Rapid initiation of guided bone regeneration driven by spatiotemporal delivery of IL-8 and BMP-2 from hierarchical MBG-based scaffold, *Biomaterials* 196 (2019) 122–137, <https://doi.org/10.1016/j.biomaterials.2017.11.011>.
- [41] M. Qu, X. Jiang, X. Zhou, C. Wang, Q. Wu, L.i. Ren, J. Zhu, S. Zhu, P. Tebon, W. Sun, A. Khademhosseini, Stimuli-responsive delivery of growth factors for tissue engineering, *Adv. Healthc. Mater.* 9 (7) (2020) 1901714, <https://doi.org/10.1002/adhm.201901714>.
- [42] B. Safari, A. Aghanejad, L. Roshangar, S. Davaran, Osteogenic effects of the bioactive small molecules and minerals in the scaffold-based bone tissue engineering, *Colloids Surf. B Biointerfaces* 198 (2021) 111462, <https://doi.org/10.1016/j.colsurf.2020.111462>.
- [43] C. Yueyi, H. Xiaoguang, W. Jingying, S. Quansheng, T. Jie, F.u. Xin, X. u. Yingsheng, S. Chunli, Calvarial defect healing by recruitment of autogenous osteogenic stem cells using locally applied simvastatin, *Biomaterials* 34 (37) (2013) 9373–9380, <https://doi.org/10.1016/j.biomaterials.2013.08.060>.
- [44] Y.-S. Liu, M.-E. Ou, H. Liu, M. Gu, L.-W. Lv, C. Fan, T. Chen, X.-H. Zhao, C.-Y. Jin, X. Zhang, Y. Ding, Y.-S. Zhou, The effect of simvastatin on chemotactic capability of SDF-1 α and the promotion of bone regeneration, *Biomaterials* 35 (15) (2014) 4489–4498, <https://doi.org/10.1016/j.biomaterials.2014.02.025>.
- [45] L. Lv, W. Ge, Y. Liu, G. Lai, H. Liu, W. Li, Y. Zhou, Lysine-specific demethylase 1 inhibitor rescues the osteogenic ability of mesenchymal stem cells under

- osteoporotic conditions by modulating H3K4 methylation, *Bone Res.* 4 (1) (2016), <https://doi.org/10.1038/boneres.2016.37>.
- [46] W. Ge, Y. Liu, T. Chen, X. Zhang, L. Lv, C. Jin, Y. Jiang, L. Shi, Y. Zhou, The epigenetic promotion of osteogenic differentiation of human adipose-derived stem cells by the genetic and chemical blockade of histone demethylase LSD1, *Biomaterials* 35 (23) (2014) 6015–6025. <http://doi: 10.1016/j.biomaterials.2014.04.055>.
- [47] K.I. Kim, S. Park, G.I. Im, Osteogenic differentiation and angiogenesis with cocultured adipose-derived stromal cells and bone marrow stromal cells, *Biomaterials* 35 (17) (2014) 4792–804. <http://doi: 10.1016/j.biomaterials.2014.02.048>.
- [48] Z. Cui, S. Kim, J. Baljon, M. Doroudgar, M. Lafleur, B.M. Wu, T. Aghaloo, M. Lee, Design and characterization of a therapeutic non-phospholipid liposomal nanocarrier with osteoinductive characteristics to promote bone formation, *ACS nano* 11 (8) (2017) 8055–8063. <http://doi: 10.1021/acsnano.7b02702>.
- [49] C.S. Li, P.u. Yang, K. Ting, T. Aghaloo, S. Lee, Y. Zhang, K. Khalilnejad, M. C. Murphy, H.C. Pan, X. Zhang, B. Wu, Y.-H. Zhou, Z. Zhao, Z. Zheng, C. Soo, Fibromodulin reprogrammed cells: A novel cell source for bone regeneration, *Biomaterials* 83 (2016) 194–206, <https://doi.org/10.1016/j.biomaterials.2016.01.013>.
- [50] J.I. González Ocampo, M.M. Machado de Paula, N.J. Bassous, A.O. Lobo, C. P. Ossa Orozco, T.J. Webster, Osteoblast responses to injectable bone substitutes of kappa-carrageenan and nano hydroxyapatite, *Acta Biomater.* 83 (2019) 425–434, <https://doi.org/10.1016/j.actbio.2018.10.023>.
- [51] M. Sadat-Shojai, M.T. Khorasani, E. Dinpanah-Khoshdargi, A. Jamshidi, Synthesis methods for nanosized hydroxyapatite with diverse structures, *Acta Biomater.* 9 (8) (2013) 7591–621. <http://doi: 10.1016/j.actbio.2013.04.012>.
- [52] G.K. Wasupalli, D. Verma, Injectable and thermosensitive nanofibrous hydrogel for bone tissue engineering, *Mater. Sci. Eng., C* 107 (2020) 110343, <https://doi.org/10.1016/j.msec.2019.110343>.
- [53] H. Zhou, J. Lee, Nanoscale hydroxyapatite particles for bone tissue engineering, *Acta Biomater.* 7(7) (2011) 2769–2781. <http://doi: 10.1016/j.actbio.2011.03.019>.
- [54] B.H. Atak, B. Buyuk, M. Huysal, S. Isik, M. Senel, W. Metzger, G. Cetin, Preparation and characterization of amine functional nano-hydroxyapatite/chitosan bionanocomposite for bone tissue engineering applications, *Carbohydr. Polym.* 164 (2017) 200–213, <https://doi.org/10.1016/j.carbpol.2017.01.100>.
- [55] C. Liu, J. Wu, D. Gan, Z. Li, J. Shen, P. Tang, S. Luo, P. Li, X. Lu, W. Zheng, The characteristics of mussel-inspired nHA/OSA injectable hydrogel and repaired bone defect in rabbit, *J. Biomed. Mater. Res. B Appl. Biomater.* 108 (5) (2019) 1814–1825. <http://doi: 10.1002/jbm.b.34524>.
- [56] Y.e. He, J. Leng, K.e. Li, K. Xu, C. Lin, Z. Yuan, R. Zhang, D. Wang, B. Tao, T. J. Huang, K. Cai, A multifunctional hydrogel coating to direct fibroblast activation and infected wound healing via simultaneously controllable photobiomodulation and photodynamic therapies, *Biomaterials* 278 (2021) 121164, <https://doi.org/10.1016/j.biomaterials.2021.121164>.
- [57] Y. Liang, J. He, B. Guo, Functional hydrogels as wound dressing to enhance wound healing, *ACS nano* 15 (8) (2021) 12687–12722. <http://doi: 10.1021/acsnano.1c04206>.
- [58] Y. Liu, Z. Zhu, X. Pei, X. Zhang, X. Cheng, S. Hu, X. Gao, J. Wang, J. Chen, Q. Wan, ZIF-8-Modified multifunctional bone-adhesive hydrogels promoting angiogenesis and osteogenesis for bone regeneration, *ACS Appl. Mater. Interfaces* 12 (33) (2020) 36978–36995, <https://doi.org/10.1021/acscami.0c12090>.
- [59] L. Han, Y. Zhang, X. Lu, K. Wang, Z. Wang, H. Zhang, Polydopamine nanoparticles modulating stimuli-responsive PNIPAM hydrogels with cell/tissue adhesiveness, *ACS Appl. Mater. Interfaces* 8 (42) (2016) 29088–29100. <http://doi: 10.1021/acscami.6b11043>.
- [60] X. Xu, B. Bai, H. Wang, Y. Suo, A near-infrared and temperature-responsive pesticide release platform through core-shell polydopamine@PNIPAm nanocomposites, *ACS Appl. Mater. Interfaces* 9 (7) (2017) 6424–6432. <http://doi: 10.1021/acscami.6b15393>.
- [61] Q. Yang, H. Yin, T. Xu, D. Zhu, J. Yin, Y. Chen, X. Yu, J. Gao, C. Zhang, Y.u. Chen, Y. Gao, Engineering 2D Mesoporous Silica@MXene-Integrated 3D-Printing Scaffolds for Combinatory Osteosarcoma Therapy and NO-Augmented Bone Regeneration, *Small* 16 (14) (2020) 1906814, <https://doi.org/10.1002/smll.v16.1410.1002/smll.201906814>.
- [62] H. Wang, X. Zeng, L. Pang, H. Wang, B. Lin, Z. Deng, E.L.X. Qi, N.a. Miao, D. Wang, P. Huang, H. Hu, J. Li, Integrative treatment of anti-tumor/bone repair by combination of MoS₂ nanosheets with 3D printed bioactive borosilicate glass scaffolds, *Chem. Eng. J.* 396 (2020) 125081, <https://doi.org/10.1016/j.cej.2020.125081>.
- [63] Y. Zhou, Y. Ni, Y. Liu, B. Zeng, Y. Xu, W. Ge, The role of simvastatin in the osteogenesis of injectable tissue-engineered bone based on human adipose-derived stromal cells and platelet-rich plasma, *Biomaterials* 31 (20) (2010) 5325–5335. <http://doi: 10.1016/j.biomaterials.2010.03.037>.
- [64] E.T. Camilleri, M.P. Gustafson, A. Dudakovic, S.M. Riester, C.G. Garces, C. R. Paradise, H. Takai, M. Karperien, S. Cool, H.-J. Sampen, A.N. Larson, W. Qu, J. Smith, A.B. Dietz, A.J. van Wijnen, Identification and validation of multiple cell surface markers of clinical-grade adipose-derived mesenchymal stromal cells as novel release criteria for good manufacturing practice-compliant production, *Stem Cell Res Ther* 7 (1) (2016), <https://doi.org/10.1186/s13287-016-0370-8>.
- [65] J. Ratanavaraporn, H. Furuya, H. Kohara, Y. Tabata, Synergistic effects of the dual release of stromal cell-derived factor-1 and bone morphogenetic protein-2 from hydrogels on bone regeneration, *Biomaterials* 32 (11) (2011) 2797–2811, <https://doi.org/10.1016/j.biomaterials.2010.12.052>.
- [66] B. Wang, Y. Guo, X. Chen, C. Zeng, Q. Hu, W. Yin, W. Li, H. Xie, B. Zhang, X. Huang, F. Yu, Nanoparticle-modified chitosan-agarose-gelatin scaffold for sustained release of SDF-1 and BMP-2, *Int. J. Nanomedicine* 13 (2018) 7395–7408, <https://doi.org/10.2147/IJN.S180859>.
- [67] J. Tan, M. Zhang, Z. Hai, C. Wu, J. Lin, W. Kuang, H. Tang, Y. Huang, X. Chen, G. Liang, Sustained release of two bioactive factors from supramolecular hydrogel promotes periodontal bone regeneration, *ACS Nano* 13 (5) (2019) 5616–5622, <https://doi.org/10.1021/acsnano.9b0078810.1021/acsnano.9b00788.s001>.
- [68] F.E. Freeman, P. Pitacco, L.H.A. van Dommelen, J. Nulty, D.C. Browe, J.Y. Shin, E. Alsborg, D.J. Kelly, 3D bioprinting spatiotemporally defined patterns of growth factors to tightly control tissue regeneration, *Sci. Adv.* 6 (33) (2020) eabb5093, <https://doi.org/10.1126/sciadv.abb5093>.
- [69] S.S. Lee, J.H. Kim, J. Jeong, S.H.L. Kim, R.H. Koh, I. Kim, S. Bae, H. Lee, N. S. Hwang, Sequential growth factor releasing double cryogel system for enhanced bone regeneration, *Biomaterials* 257 (2020) 120223, <https://doi.org/10.1016/j.biomaterials.2020.120223>.
- [70] R.T. Annamalai, P.A. Turner, W.F. Carson, B. Levi, S. Kunkel, J.P. Stegemann, Harnessing macrophage-mediated degradation of gelatin microspheres for spatiotemporal control of BMP2 release, *Biomaterials* 161 (2018) 216–227, <https://doi.org/10.1016/j.biomaterials.2018.01.040>.
- [71] N. Chen, R. Ren, X. Wei, R. Mukundan, G. Li, X. Xu, G. Zhao, Z. Zhao, S.M. Lele, R. A. Reinhardt, D. Wang, Thermoresponsive Hydrogel-Based Local Delivery of Simvastatin for the Treatment of Periodontitis, *Mol. Pharmaceutics* 18 (5) (2021) 1992–2003, <https://doi.org/10.1021/acs.molpharmaceut.0c01196>.
- [72] E. Metzger, M. Wissmann, N. Yin, J.M. Müller, R. Schneider, A.H. Peters, T. Günther, R. Buettner, R. Schüle, LSD1 demethylates repressive histone marks to promote androgen-receptor-dependent transcription, *Nature* 437 (7057) (2005) 436–439. <http://doi: 10.1038/nature04020>.
- [73] S. Pauly, F. Luttsch, M. Morawski, N.P. Haas, G. Schmidmaier, B. Wildemann, Simvastatin locally applied from a biodegradable coating of osteosynthetic implants improves fracture healing comparable to BMP-2 application, *Bone* 45 (3) (2009) 505–511. <http://doi: 10.1016/j.bone.2009.05.01>.
- [74] H.T. Lee, M.R. Choi, M.S. Doh, K.H. Jung, Y.G. Choi, Effects of the monoamine oxidase inhibitors pargyline and tranylcypromine on cellular proliferation in human prostate cancer cells, *Oncol. Rep.* 30 (4) (2013) 1587–1592, <https://doi.org/10.3892/or.2013.2635>.
- [75] S.J. Hogg, P.A. Beavis, M.A. Dawson, R.W. Johnstone, Targeting the epigenetic regulation of antitumor immunity, *Nat. Rev. Drug Discov.* 19 (11) (2020) 776–800, <https://doi.org/10.1038/s41573-020-0077-5>.
- [76] M.A. Dawson, T. Kouzarides, Cancer epigenetics: from mechanism to therapy, *Cell* 150 (1) (2012) 12–27. <http://doi: 10.1016/j.cell.2012.06.013>.
- [77] R.J. Sims, 3rd, K. Nishioka, D. Reinberg, Histone lysine methylation: a signature for chromatin function, *Trends. Genet.* 19 (11) (2003) 629–639. <http://doi: 10.1016/j.tig.2003.09.007>.
- [78] A. Portela, M. Esteller, Epigenetic modifications and human disease, *Nat. Biotechnol.* 28 (10) (2010) 1057–1068. <http://doi: 10.1038/nbt.1685>.
- [79] C. Qu, Z. Bao, X. Zhang, Z. Wang, J. Ren, Z. Zhou, M. Tian, X. Cheng, X. Chen, C. Feng, A thermosensitive RGD-modified hydroxybutyl chitosan hydrogel as a 3D scaffold for BMSCs culture on keloid treatment, *Int. J. Biol. Macromol.* 125 (2019) 78–86, <https://doi.org/10.1016/j.ijbiomac.2018.12.058>.
- [80] X. Zhang, M. Kong, M. Tian, C. Qu, J. Li, Y.N. Wang, Q. Sun, X. Cheng, X. Chen, The temperature-responsive hydroxybutyl chitosan hydrogels with polydopamine coating for cell sheet transplantation, *Int. J. Biol. Macromol.* 120 (Pt A) (2018) 152–158, <https://doi.org/10.1016/j.ijbiomac.2018.08.015>.
- [81] M. Sun, D. Qin, P. Fan, X. Chen, Y. Liu, Chitosan-centered nanosystems as sustained therapeutics for allergic rhinitis intervention: Inhibition of histamine-induced cascades, *J. Control Release* 335 (2021) 422–436, <https://doi.org/10.1016/j.jconrel.2021.05.048>.
- [82] T. Lim, Q. Tang, Z. Zhu, X. Wei, C. Zhang, Sustained release of human platelet lysate growth factors by thermosensitive hydroxybutyl chitosan hydrogel promotes skin wound healing in rats, *J. Biomed. Mater. Res. A* 108 (10) (2020) 2111–2122, <https://doi.org/10.1002/jbm.a.36970>.
- [83] X. Liu, S. Song, J. Huang, H. Fu, X. Ning, Y. He, Z. Zhang, HBC-nanofiber hydrogel scaffolds with 3D printed internal microchannels for enhanced cartilage differentiation, *J. Mat. Chem. B* 8 (28) (2020) 6115–6127, <https://doi.org/10.1039/d0tb00616e>.
- [84] C. Li, K. Wang, X. Zhou, T. Li, Y. Xu, L. Qiang, M. Peng, Y. Xu, L. Xie, C. He, B. Wang, J. Wang, Controllable fabrication of hydroxybutyl chitosan/oxidized chondroitin sulfate hydrogels by 3D bioprinting technique for cartilage tissue engineering, *Biomed. Mater.* 14 (2) (2019), 025006, <https://doi.org/10.1088/1748-605X/aaf8ed>.
- [85] Q. Feng, J. Xu, K. Zhang, H. Yao, N. Zheng, L. Zheng, J. Wang, K. Wei, X. Xiao, L. Qin, L. Bian, Dynamic and cell-infiltratable hydrogels as injectable carrier of therapeutic cells and drugs for treating challenging bone defects, *ACS Cent. Sci.* 5 (3) (2019) 440–450.
- [86] J. Whitehead, K.H. Griffin, M. Gionet-Gonzales, C.E. Vorwald, S.E. Cinque, J. K. Leach, Hydrogel mechanics are a key driver of bone formation by mesenchymal stromal cell spheroids, *Biomaterials* 269 (2021), 120607, <https://doi.org/10.1016/j.biomaterials.2020.120607>.
- [87] M. Zhang, Q. Sun, Y. Liu, Z. Chu, L. Yu, Y. Hou, H. Kang, Q. Wei, W. Zhao, J. P. Spatz, C. Zhao, E.A. Cavalcanti-Adam, Controllable ligand spacing stimulates cellular mechanotransduction and promotes stem cell osteogenic differentiation on soft hydrogels, *Biomaterials* 268 (2021) 120543, <https://doi.org/10.1016/j.biomaterials.2020.120543>.
- [88] W. Yuan, H. Wang, C. Fang, Y. Yang, X. Xia, B. Yang, Y. Lin, G. Li, L. Bian, Microscopic local stiffening in a supramolecular hydrogel network expedites stem

- cell mechanosensing in 3D and bone regeneration, *Mater. Horiz.* 8 (6) (2021) 1722–1734, <https://doi.org/10.1039/d1mh00244a>.
- [89] X. Bai, Z. Bao, S. Bi, Y. Li, X. Yu, S. Hu, M. Tian, X. Zhang, X. Cheng, X. Chen, Chitosan-based thermo/pH double sensitive hydrogel for controlled drug delivery, *Macromol. Biosci.* 18 (3) (2018) 1700305, <https://doi.org/10.1002/mabi.201700305>.
- [90] E. Zhang, Q. Guo, F. Ji, X. Tian, J. Cui, Y. Song, H. Sun, J. Li, F. Yao, Thermoresponsive polysaccharide-based composite hydrogel with antibacterial and healing-promoting activities for preventing recurrent adhesion after adhesiolysis, *Acta Biomater.* 74 (2018) 1264–1270, <https://doi.org/10.1016/j.actbio.2018.05.037>.
- [91] J. Li, Q. Shi, X. Wu, C. Li, X. Chen, *In vitro* and *in vivo* evaluation of 3D biodegradable thermo/pH sensitive sol-gel reversible hydroxybutyl chitosan hydrogel, *Mater. Scia Eng. C Mater. Biol. Appl.* 108 (2020) 110419, <https://doi.org/10.1016/j.msec.2019.110419>.
- [92] X. Zhang, W. Jiang, Y. Liu, P. Zhang, L. Wang, W. Li, G. Wu, Y. Ge, Y. Zhou, Human adipose-derived stem cells and simvastatin-functionalized biomimetic calcium phosphate to construct a novel tissue-engineered bone, *Biochem. Biophys. Res. Commun.* 495 (1) (2018) 1264–1270, <https://doi.org/10.1016/j.bbrc.2017.11.150>.
- [93] F. Salehpour, P. Cassano, N. Rouhi, M.R. Hamblin, L. De Taboada, F. Farajdokht, J. Mahmoudi, Penetration profiles of visible and near-infrared lasers and light-emitting diode light through the head tissues in animal and human species: A review of literature, *Photobiomodul. Photomed. Laser Surg.* 37 (10) (2019) 581–595, <https://doi.org/10.1089/photob.2019.4676>.
- [94] A. Saneja, R. Kumar, D. Arora, S. Kumar, A.K. Panda, S. Jaglan, Recent advances in near-infrared light-responsive nanocarriers for cancer therapy, *Drug Discov. Today* 23 (5) (2018) 1115–1125, <https://doi.org/10.1016/j.drudis.2018.02.005>.
- [95] J.F. Gohy, Y. Zhao, Photo-responsive block copolymer micelles: design and behavior, *Chem. Soc. Rev.* 42(17) (2013) 7117–7129. <http://doi: 10.1039/c3cs35469e>.
- [96] C. Yang, H. Ma, Z. Wang, M.R. Younis, C. Liu, C. Wu, Y. Luo, P. Huang, 3D printed wesselsite nanosheets functionalized scaffold facilitates NIR-II photothermal therapy and vascularized bone regeneration, *Adv. Sci. (Weinh)* 8 (20) (2021), e2100894, <https://doi.org/10.1002/advs.202100894>.
- [97] J. Wu, L. You, L.u. Lan, H.J. Lee, S.T. Chaudhry, R. Li, J.-X. Cheng, J. Mei, Semiconducting Polymer Nanoparticles for Centimeters-Deep Photoacoustic Imaging in the Second Near-Infrared Window, *Adv. Mater.* 29 (41) (2017) 1703403, <https://doi.org/10.1002/adma.v29.4110.1002/adma.201703403>.
- [98] T. He, C. Jiang, J. He, Y. Zhang, G. He, J. Wu, J. Lin, X. Zhou, P. Huang, Manganese-dioxide-coating-instructed plasmonic modulation of gold nanorods for activatable duplex-imaging-guided NIR-II photothermal-chemodynamic therapy, *Adv. Mater.* 33 (13) (2021), e2008540, <https://doi.org/10.1002/adma.202008540>.
- [99] W. Zhao, Y. Zhao, Q. Wang, T. Liu, J. Sun, R. Zhang, Remote light-responsive nanocarriers for controlled drug delivery: advances and perspectives, *Small* 15 (45) (2019), e1903060, <https://doi.org/10.1002/smll.201903060>.
- [100] C.G. Dariva, J.F.J. Coelho, A.C. Serra, Near infrared light-triggered nanoparticles using singlet oxygen photocleavage for drug delivery systems, *J. Control. Release* 294 (2019) 337–354, <https://doi.org/10.1039/c8cs00618k>.
- [101] Y. Liu, P. Bhattarai, Z. Dai, X. Chen, Photothermal therapy and photoacoustic imaging via nanotheranostics in fighting cancer, *Chem. Soc. Rev.* 48 (7) (2019) 2053–2108. <http://doi: 10.1039/c8cs00618k>.
- [102] J. Son, G. Yi, J. Yoo, C. Park, H. Koo, H.S. Choi, Light-responsive nanomedicine for biophotonic imaging and targeted therapy, *Adv. Drug Deliv. Rev.* 138 (2019) 133–147, <https://doi.org/10.1016/j.addr.2018.10.002>.
- [103] S. Luo, J. Wu, Z. Jia, P. Tang, J. Sheng, C. Xie, C. Liu, D. Gan, D. Hu, W. Zheng, X. Lu, An injectable, bifunctional hydrogel with photothermal effects for tumor therapy and bone regeneration, *Macromol. Biosci.* 19 (9) (2019) 1900047, <https://doi.org/10.1002/mabi.201900047>.
- [104] Y. Wang, Q. Huang, X. He, H. Chen, Y. Zou, Y. Li, K. Lin, X. Cai, J. Xiao, Q. Zhang, Y. Cheng, Multifunctional melanin-like nanoparticles for bone-targeted chemophotothermal therapy of malignant bone tumors and osteolysis, *Biomaterials* 183 (2018) 10–19, <https://doi.org/10.1016/j.biomaterials.2018.08.033>.
- [105] S. Sanchez-Casanova, F.M. Martin-Saavedra, C. Escudero-Duch, M.I. Falguera Uceda, M. Prieto, M. Arruebo, P. Acebo, M.L. Fabiilli, R.T. Franceschi, N. Vilaboa, Local delivery of bone morphogenetic protein-2 from near infrared-responsive hydrogels for bone tissue regeneration, *Biomaterials* 241 241 (2020) 119909, <https://doi.org/10.1016/j.biomaterials.2020.119909>.
- [106] H. Lee, S.M. Dellatore, W.M. Miller, P.B. Messersmith, Mussel-Inspired Surface Chemistry for Multifunctional Coatings, *Science* 318 (5849) (2007) 426–430, <https://doi.org/10.1126/science.1147241>.
- [107] Y. Meng, P. Liu, W. Zhou, J. Ding, J. Liu, Biorthogonal DNA adsorption on polydopamine nanoparticles mediated by metal coordination for highly robust sensing in serum and living cells, *ACS nano* 12(9) (2018) 9070–9080. <http://doi: 10.1021/acsnano.8b03019>.
- [108] Y. Xue, W. Niu, M. Wang, M. Chen, Y. Guo, B. Lei, Engineering a biodegradable multifunctional antibacterial bioactive nanosystem for enhancing tumor photothermo-chemotherapy and bone regeneration, *ACS nano* 14(1) (2020) 442–453. <http://doi: 10.1021/acsnano.9b06145>.
- [109] G. Gao, Y.-W. Jiang, H.-R. Jia, F.-G. Wu, Near-infrared light-controllable on-demand antibiotics release using thermo-sensitive hydrogel-based drug reservoir for combating bacterial infection, *Biomaterials* 188 (2019) 83–95, <https://doi.org/10.1016/j.biomaterials.2018.09.045>.
- [110] J.N. Tiwari, Y.K. Seo, T. Yoon, W.G. Lee, W.J. Cho, M. Yousuf, A.M. Harzandi, D. S. Kang, K.Y. Kim, P.G. Suh, K.S. Kim, Accelerated Bone Regeneration by Two-Photon Photoactivated Carbon Nitride Nanosheets, *ACS nano* 11(1) (2017) 742–751. <http://doi: 10.1021/acsnano.6b07138>.
- [111] X. Zhang, G.u. Cheng, X. Xing, J. Liu, Y. Cheng, T. Ye, Q. Wang, X. Xiao, Z. Li, H. Deng, Near-infrared light-triggered porous AuPd alloy nanoparticles to produce mild localized heat to accelerate bone regeneration, *J. Phys. Chem. Lett.* 10 (15) (2019) 4185–4191, <https://doi.org/10.1021/acs.jpclett.9b01735>.
- [112] L. Tong, Q. Liao, Y. Zhao, H. Huang, A. Gao, W. Zhang, X. Gao, W. Wei, M. Guan, P.K. Chu, H. Wang, Near-infrared light control of bone regeneration with biodegradable photothermal osteoimplant, *Biomaterials* 193 (2019) 1–11, <https://doi.org/10.1016/j.biomaterials.2018.12.008>.